Influence of large scale breaking waves in the near field of ships

Author: Fabrizio Pistani
Tutor: Renzo Piva
Guiding professor: Emilio Campana

Philosophy Doctor Thesis XVI Cycle

University of Roma *La Sapienza* - Faculty of Engineering

Ai miei Genitori, ancora una volta devo tutto a loro

E al mio Fratellino che sulle onde ci vive davvero

Pura Vida;

A Monica per il suo amore e il suo supporto;

Agli Amici e ai Compagni,

A Chi mi ha insegnato ad imparare,

grazie a tutti ancora una volta.

Contents

1 Introduction

Wave breaking is a commonly experienced phenomena at sea. Breakers can be seen as waves approach to the beach, around the surface piercing pillars of piers and platforms, around moving or moored ships. Waves can also break without any interaction with solid bodies under the influence of wind gusts or because of the superposition of more than one wave. Wave breaking is an important mechanism for the exchange of heat and oxygen between ocean and atmosphere through the water surface and when a wave breaks around the ship its drag is influenced, air bubbles are entrapped in its wake, the noise increases. For coastal and structural engineering is important to evaluate the loads due to wave breaking. For these and many other reasons waves that break have been the object of many experimental, numerical and theoretical studies.

The Subject of this Ph.D Thesis is wave breaking of ships, focusing in particular with the near field of ships. The first steps of this activity started in 1996 from a project of professor F.Stern from IIHR (Iowa Institute of Hydraulic Research) carried on in collaboration with INSEAN (Istituto Studi ed Esprienze di Architettura Navale), the laboratory where the measurements of this work have been done. The main objectives were a better understanding of the complex flow physics around ships with the idea that the measured data would be also useful for CFD validation. This Thesis takes inspiration from that activity providing an additional study at larger scale. Some of the data collected in those occasions will be here utilized to make the comparison with present measurements.

1.1 Topology of the breaker

The main characteristics of a breaking wave have been described and formalized by many authors. Systematic descriptions can be found, among many others, in [2] and [15] and the same terminology will be adopted in this thesis.

A wave, in breaking conditions, loses the symmetry that characterizes the sinusoidal waves. The forward face of the wave increases its steepness up until the point where breaking happens. Then, distintion has to be made between long and short waves. At small scale a train of capillary waves can be seen stationary with the breaking wave on its forward face (figure 1). Reports on researches that focus specifically on

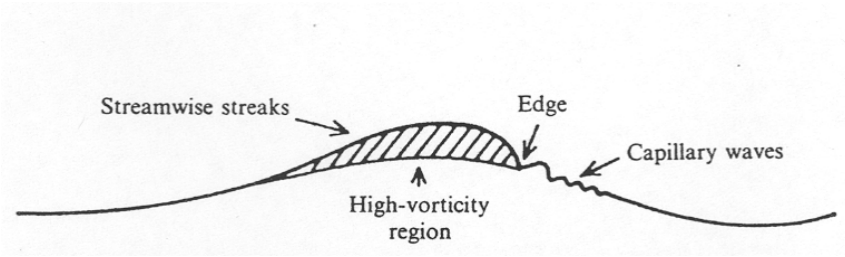

Figure 1: drawing taken from [28] showing the capillary wave train in front of the forward face of the breaker.

this train of capillary waves with the aim of understanding its role on the breaking can be found in [28], [31], [5] and in the more general reviews of Dias et al. [9] and Perlin et al. [33]. At the moment of breaking the wave crest suddenly brakes down, its surface looses smoothness and regularity, and a mass of water literally slides bubbling down the face of the wave. From this moment the wave propagates in a new quasi steady configuration that can be described as a *bulge* of turbulent water riding the forward face of the wave. The point were this bulge encounters the smooth water surface is commonly addressed as the *toe* of the wave (figure 2). This breaking configuration is called *spilling breaker*.

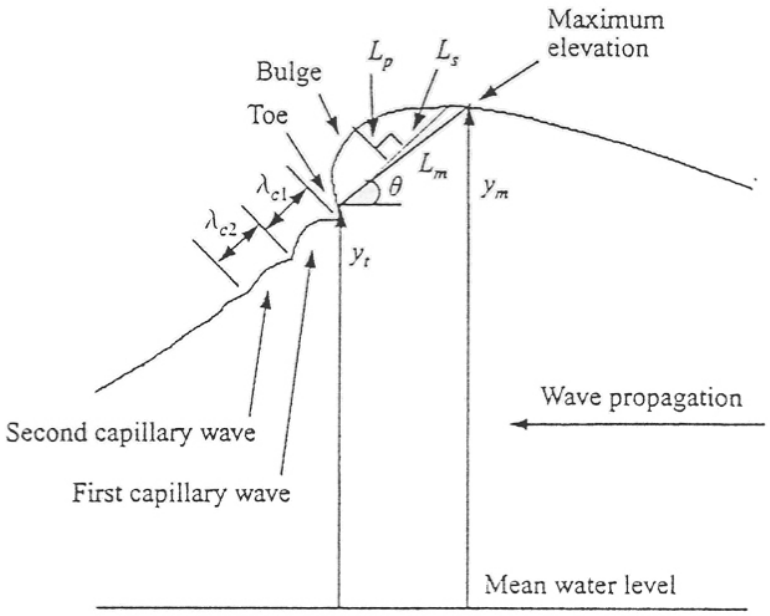

Figure 2: illustration of the nomenclature used for breaking waves from Duncan [15].

There can be other cases, for example when the waves are big enough, or there is a superface force, like the one exerted by the wind, that counteracts the advancing motion of the wave, where the breaking process initiates with a turning motion of the peak of the wave, that eventually falls as a jet in the upstream water (figure 3). This jet entering the water gives origin to a splash up that can generate another one and so on, till there is enough energy for this process. This breaking is known as *plunging breaker*.

Indipendently of how the breaking has started the wave train can reach the statistically steady configuration in which the height of the first breaking crest is lower than in the non breaking configuration, and the bulge rides on the forward face, whereas the entire following waves are damped out.

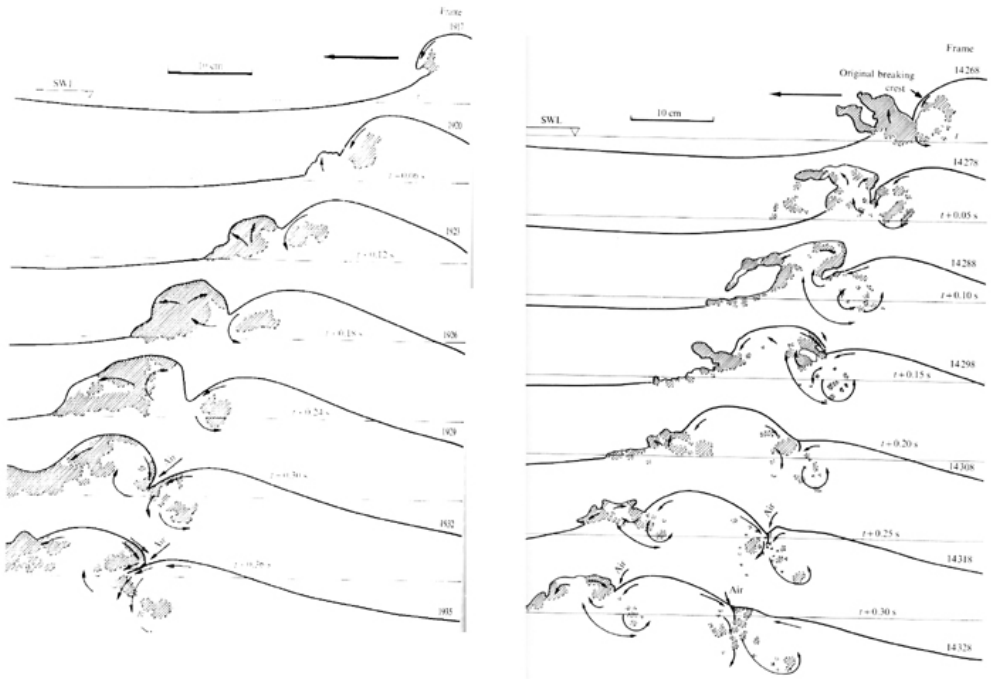

Figure 3: Bonmarin [3] illustrates the sequence of a plunging type breaker.

1.2 2D laboratory wave breaking

Duncan has been one of the pioneers in attempting to reproduce experimental wave breaking in laboratory. Since 1981 he started a series of experiments on 2D waves focused in understanding the process of initiation and evolution of breaking. In [11] the wave was produced by towing a submerged hydrofoil at constant speed and depth in a calm water channel. It was one of the first attempts to individuate the parameters for describing the asymmetric breaking wave. The breaking does not only modifies the shape of the wave but it is also a source of energy dissipation that can be put in relation to the breaking itself. The drag associated to a breaking and to a non breaking 2D wave was calculated from measurements of velocity and free surface elevation by Duncan [12] showing an increase in drag up to three times the drag associated to the non breaking wave.

This increase in resistance due to the wave breaking was already a topic of interest in the naval field. In 1969 Baba [1] reported of a new component of ship resistance

that originates in the dissipation of energy due to *breakdown of bow waves*, pointing out that this component can not be quantified with the traditional methods of wave resistance components derived from wave analysis.

With a few exceptions, the majority of laboratory experiments have been carried out with 2D breaking waves, mostly because these are more easy to be generated and controlled. The breaker can be generated by a moving obstacle under the free surface, or by making use of the dispersion properties of the water waves for focusing in space a train of waves, with different wavelength, generated by a wavemaker.

The research on waves can be divided into two main areas [14], one exploring the overall dynamics of the wave by determining the incipient breaking conditions and the drag associated with the breaking and the other interested in the surface height fluctuations, the characterization of their amplitude, frequency, wavelength and the downstream propagation of the disturbances.

In 1989 Bonmarin [3] reported observations of the shape evolution of a plunging crest, its following splash up in the undisturbed upstream water surface and the consequent air entrapment. They used a visualization technique to freeze the wave during its evolution towards breaking and measure the variation of geometry: the number of geometric parameters necessary to describe the shape of a steep progressive wave increases from the simple sinusoidal to the breaking case. Rapp and Melville in 1990 [39] measured, with laser doppler anemometry technique, the flow velocity of a breaker obtained with the focusing technique: a train of waves of decreasing frequency was generated by the wavemaker so to meet and concentrate in a established point in space. They calculated the momentum loss due to wave breaking and survey the evolution of the turbulent wake.

One of the most discussed topics is the dynamic of the bulge of the wave and the role of the capillary wave train in front of the main crest of the breaker. Longuet-Higgins in 1992 [28] demonstrated theoretically that vorticity is produced by the capillary wave train in front of the gravity wave crest simply because of the geometrical cur-

vature of the free surface and in [29] focused on the instabilities due to the capillary wave trains that are of two types and finds a relation between their wavelengths. Duncan et al. in 1994 [13] presented pictures of the evolution of a spilling breaker till the flow becomes turbulent. This topic was explored also in [6] with more attention to the scale effect using hydrofoils of varying dimensions and in [14] the spectrum of the fluctuating surface was measured from the time history of the surface elevation at a fixed point.

More detailed measurements of the flow under the breaking waves with the intent of characterizing also the vorticity field where carried out by various authors, see [8] [4] and [32], using PIV systems. In these series of works becomes evident that the breaking phenomenon is originated from the interaction of a surface shear layer with the potential flow of the regular wave and the whole process is confined to a very thin area close to the surface. In particular the work of Chang and Liu was dealing with a plunging breaker with overturning crest and they also measured the velocity of the jet when impinges the water in front of the crest. Dabiri and Gharib [8] measured that the dominant source of the vorticity flux into the flow is to be found in the free surface deceleration. Lastly in two works [15] and [16] Duncan and colleagues explore both the surface and the flow of a spilling breaker again confirming the source of vorticity in the shear layer between the breaking bulge and the underneath wave.

Efforts for proposing models for the wave breaking were carried out by Cointe and Tulin in 1994 [7], their model was deduced from the observation of 2D breakers and consists of a stagnant eddy riding on the forward face of leading wave of the wave train behind the hydrofoil.

1.3 3D wave breaking and ship breaking waves

Most of laboratory experiments have been performed on 2D spilling breakers. Indeed these kind of breakers are more easy to generate and control. Furthermore the spilling breaker flow can be considered as a *steady* breaker [2]. Plunging breakers and three dimensional breaking waves are more common in nature and in technological applications but much more difficult to reproduce and to study.

Three dimensional wave breaking is a common event in the free surface in the proximity of the solid wall of ships and the flow characteristics around ships are essentially three dimensional. These subjects have received increasing attention by the scientific community in the last years and the conclusions relative to accurate measurements and numerical simulations have been reported in the workshop of *Gothenburg 2000* [24] and in [25].

In a review of 1984 Miyata and Inui [30] illustrate the characteristics of the waves produced by ships. Two major non linear waves are produced by the forward part of a ship when advancing, the so called bow and shoulder wave. The crest line of the bow wave is nearly parabolic and the shoulder wave has a straight crest. The free surface evolution is illustrated mainly by pictures and visual observation, measurements of the flow by means of Pitot probe are reported. The authors lamented the inadequacy of the linear wave making theories in predicting the ship resistance pointing out the fact that the wave pattern around a ship cannot anymore be considered simply as a linear wave pattern, but modern ship research had to start taking into consideration the breaking of the waves in the near field, as it had been highlighted by Baba in 1969 [1]. Later Larsson and Baba formalized their findings in a paper that classifies all the different components that contribute to the total resistance of a ship [23] bringing into attention that, for certain kind of ships, is the resistance due to wave breaking that plays the major role. Pogozelski at al. in 1996 [38] reported their measurements of the shoulder wave of a simplified case of a surface piercing strut of symmetrical shape presenting plots of velocity and calculations of vorticity.

Also this simple shaped test case produces a wave pattern composed of a bow and shoulder wave. The wake of the bow wave creates a turbulent flow that influences the evolution of the following shoulder wave and vorticity is generated also at the boundary between the free surface and the solid wall of the model where, behind the shoulder wave, the flow separates. One year later the measurements on a ship model bow wave where published [10]. The model was 3.05 meters long and without bow bulb. The work focused on the thin sheet of water where the bow wave originates from and where there is a considerable production of vorticity that is convected downstream into the flow around the model. Due to the limited dimensions of the model the near wave field was influenced by surface tension and for low Froude numbers the bow wave was not breaking. By increasing Froude number a very mild spilling type breaker was generated. The same topic was resumed in [40], where the authors measured with the PIV the flow around a longer model (7 $m.$) with a bow bulb in different sections, trying to follow the evolution of the vorticity generated in the thin sheet of water that climbs the inclined side of the bow. They also calculated the Reynolds stresses from the two velocity components measurable with the PIV, confirming the turbulent nature of the wake of the wave and addressing the toe of the breaker as the region of turbulent production.

When the bow of a ship passes it perturbs the water surface and generates the waves, a breaking bow wave is continuously generated and a splash up is continuously happening. Then the waves propagate at a certain angle with respect to the advancing direction of the ship.

The disturb generated by the splash up of the wave crest propagates at the same angle and parallel to the crest that gave origin to it. This is an area of intense vorticity (in analogy with a jet entering the water) and its effect on the free surface is the presence of line on the surface where continuity is lost and water is pull down by the vortices with axis parallel to the free surface. The scientific literature now commonly refers to these surface signs as *scars*. Being locations of vortical activity

in close contact to the free surface this scars can entrap air from the surface, the air remains trapped in the vortex core and white filaments can be seen under the water surface (figure 4). The air will emerge downstream under the form of bubbly wake.

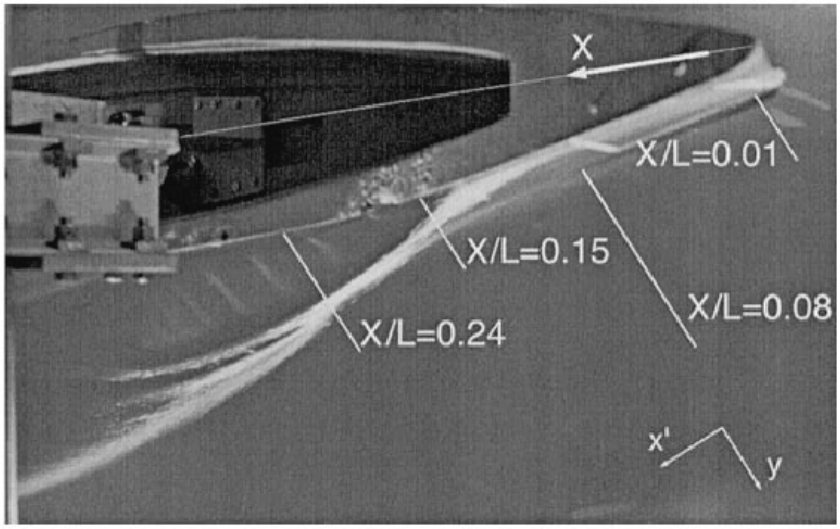

Figure 4: from the paper of Dong at al. [10] *" note that the streaks in figure, beyond the $X/L = 0.24$ line, have been created by entrained bubbles".*

Measurements of the flow by means of Pitot probe and of the near field wave elevation, together with a comparison between experimental and numerical data is reported in [35], where surface scars in the wake of the wave field are addressed as the consequence of the vorticity generated at the bow wave splash ups.
Wave pattern was also measured in more complicated conditions by Gui et al. [19] where a 3.048 meters long model was towed in regular head waves.
Previously cited papers dealing with 3D ship waves consider restricted areas of the bow, [37] for the first time extends accurate measurements to a wide zone surrounding the hull that is influenced by the breaking waves and their wakes, reporting analysis of the mean flow measured on several transversal sections and a wave elevation map with mean and rms values extended to over the 50% of the hull's length.

Furthermore this papers couples wave elevation patterns relative to the far and the near field, provides analysis of the vorticity in the flow and about its relationship with the observed features of the free surface. In addition an extensive photo study of the flow around the models comparisons with the real ship is displayed. Finally comparisons with CFD results can be found.

The need of more detailed data of the wave pattern becomes evident also to be used as validation tests for numerical solutions. At present numerical codes for simulating breaking conditions face the difficulty of the great resolution needed to describe the process of breaking that involves very small scale dynamics. In order to ease the comparisons with numerical data from simulations more detailed and complete data for ship models was collected by Stern et al. utilizing a modern hull model with bulb and transom stern and reported in [42] and [34]. Scale effects were reported for resistance test in [42], a small model compared to a larger one had similar residual resistance values in the low Froude range while for high Froude numbers the residual resistance of the small model was sensibly lower. In that work the authors report a difference in the wave pattern and in the wave breaking between a model of 3 meters of length and another 5.7 meters long. Finally detailed free surface, pressure and flow maps are reported in [26] by Longo and Stern for a model with non zero drift angle.

The dynamic and evolution of three dimensional breakers differs from the two dimensional case. The latter can be a laboratory test case very useful in understanding the basics of the crest evolution and the initiation of the breaking process but the vorticity and the turbulent wake have a different evolution in 3D.

As an example one can observe the 3D wave pattern produced by a ship, stationary with the ship itself. Even if the precise configuration of the waves depends on the velocity of the ship, the pattern typically includes two highly non linear waves, namely the bow wave and shoulder wave, almost invariably in breaking conditions at full scale dimensions. It is quite clear whereas in a 2D breaker the vorticity produced

at the toe is transported downstream by the flow and far from the crest, for a 3D breaker the vorticity is convected in a series of vortex filaments that remain close to the wave crest [10].

When decreasing the dimensions of the object that produces the waves the Froude law of similarity ensures that it is possible to satisfy the conditions for having a similar far field wave pattern for the real case and for the scaled one. This condition is the equality of the Froude number for the two scales.

Following this consideration [37] explores the flow features around ship models at two different scales of the same model geometry that will be here adopted and provides explanation about free surface particular features.

The present Thesis has the objective of providing an extension towards an even larger model dimension in order to give further impulse providing a set of experimental results and analysis more closely related to the full scale phenomena.

Comparing pictures taken on real ships and on scaled models it is possible to see that when the Froude law of similarity is satisfied the far wave fields are similar but the near fields are very different, see figure 5. The bow wave of the real ship is in breaking conditions with overturning crest, production of white water and spray and ejection of drops. Most of these phenomena are not seen, or happen in a mild form, on model scales. This fact is due to the increasing role of surface tension as a restoring force as the scale of the wave decreases. In particular for waves of wave length less than about a few meters the effect of the surface tension becomes increasingly visible eventually resulting in the suppression of the overturning jet for waves of length less than about 50 cm., although breaking still occurs [43] [17]. Indeed wave length plays an important role in determining the behavior of the breaking waves: as the wave length decreases *"the jet or droplet formation is influenced by surface tension and, for short waves, is replaced by surface tension dominated ripple pattern on the forward face of the crest"* [17]. Surface tension enters the equations of motion through the dynamic free surface boundary condition, the pressure jump term in

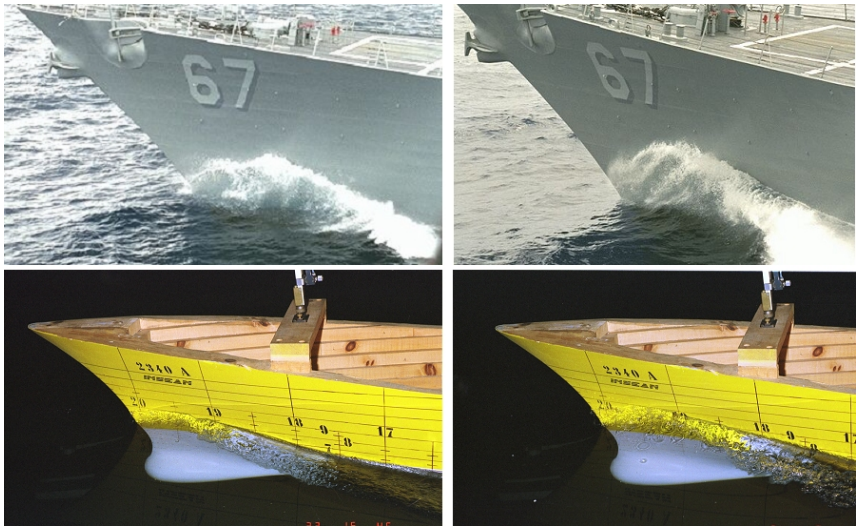

Figure 5: comparison of the non linear bow wave between a full scale ship and a model scaled $\lambda = 24.824$ towed at the same Froude number. Full scale ship sailing at 20 knots (left) corresponding to Froude 0.28 and at 25 knots (right) equivalent to Froude 0.35. Pictures taken from [37].

the equation of motion includes a term in the form of T/r, where T is the surface tension and r is the radius of the curvature of the free surface, when dimensions are smaller curvature radius increases and the importance of the term grows.

Thus the key for governing surface tension effects is the control on the geometrical properties of the wave.

The aim of this work is a better understanding of the influence of the breaking waves in the near field of the ships and an evaluation of the differences in the energy dissipation between breaking waves of dimensions that are common for towing tank test models and waves can be considered as more resemblant to the full scale breaking waves. Since the breaker perturbs differently the near field as its dimensions change its influence has to be sought in the field itself.

The rationale of the thesis is to overcome the limits that inhibit a full breaking dynamic at the common model dimensions by using a very large model so to have a laboratory test case without the decisive influence of the surface tension in the

near wave field. A comparison between the data taken at the large scale with the data acquired during the previous activity ([34], [35] and [37]) will provide useful information for a better estimate of the full scale.

The approach used in the present work consists in a series of experiments set up with the same methodology and measurement systems used in [37]: the generation and measurement of ship waves by using identical models of different scales, in order to compare the wave fields and single out the differences that can be attributed to the different breaking behavior; the measurement of the mean flow field over selected transversal sections, in order to analyze the flow immediately under the breaking wave activity; the point to point survey of the wave elevation in order to obtain a complete description and possibly identify singular features as the breaking areas and the scars; an accurate photo study, in order to highlight the importance of the dimensions of the waves. All the tests of this Thesis have been carried out in the same facility so to isolate only those phenomena relative to the different scale of the models.

1.4 Thesis Layout

The thesis is organized as follows, in the second chapter the requirements of the test will be put in evidence, the process for the choice of the ideal conditions of test will be described and the physical quantities and areas of interests will be established.

The third chapter is dedicated to illustrate the measuring procedures and methods, the design and engineering of the test is described putting in evidence the solutions adopted, a description of the instruments will be provided.

The fourth chapter provides the description of the comparison between three scales of the model towed for a complete range of conditions of interest. Photographic images and data about the resistance will be reported and discussed.

The fifth chapter focus on one significant condition and local measurements of the

wave elevation and mean velocity flow in the near field of a large scale model. The second part of the chapter will report comparisons between data collected for a smaller scale in the same conditions.

Finally the conclusions will be presented in the sixth chapter.

Figure 6: Parc Güell, Gaudi's masterwork in Barcellona, Spain, is one of the best examples of how breaking and overturning crest of waves can be eye-catching not only for researchers.

2 Tests Design

As it has been discussed in the previous chapter the steady ship waves are are a good example of highly reproducible 3D breaker. Great experience has been gathered during the past years in ship model testing. From the almost empirical attitude of the beginnings of the century, when a ship that looked beautiful had to be a good ship, the procedures, the instruments and the analysis are updated and modernized year by year .

Thus a scaled ship model, towed in a rectilinear basin facility, was chosen for producing the waves object of this study. The test speed had to be chosen in order to make comparisons with similar measurements performed at different scales. The first step in the designing of the experiment has been the assessment of the dimensions of the model apt to produce waves that showed a fully developed breaking as similar as possible to the breaking waves of a real ship. In order to show a fully developed breaking the wavelength has to be $\lambda \geq 0.50\ m$ (see [43]).

In order to compare the wave patterns produced by models of different dimensions the test speed has to satisfy the Froude law of similarity that states that two geometrically similar bodies of different scales will produce a wave pattern that is geometrically similar if their velocities are such that satisfy the following relationship:

$$\frac{v_M}{v_S} = \sqrt{\frac{L_S}{L_M}}, \tag{1}$$

where M stays for model and S for real scale ship, v is the velocity and L is a characteristic dimension, very often in ship model testing the length between per-

pendiculars L_{PP} is used. Said in a different way, relation 1 states that the Froude number, defined as:

$$Fr = \frac{v}{\sqrt{gL}} \tag{2}$$

must have the same value for the model and for the ship.

The wavelength of the wave pattern produced by a body moving on the water surface is proportional to the characteristic length of the model.

Photographic studies carried out for real ships and for models showed that the most interesting wave breaking formations around the hull happen on the bow wave crest and on the shoulder wave crest. The areas of interest are the crests of these two waves together with their fronts and wakes. The underneath flow is also influenced by the wave presence and by the breaking. The pictures shot at different speeds for a combattant ship with bulb and for its scaled models show that there are regimes of developed breaking. One of these conditions was chosen for measuring the wave pattern, the velocity flow and the resistance force.

For comparisons with other scales the geometry chosen for the model is the DDG51 ship which lines are shown in figure 7. DDG51 is a fast displacement ship of modern

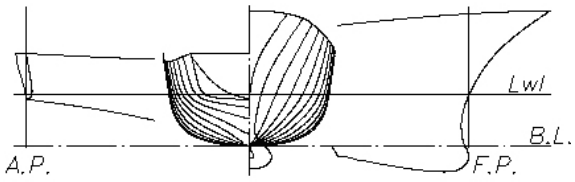

Figure 7: construction lines of DDG51 and models.

conception. This ship has a transom stern and the a bow bulb of peculiar shape, round at the beginning and flat and horizontal at the end that is used to host the sonar in the real ship. This geometry was recommended by the International Towing Tank Conference (ITTC) since 1996 as a benchmark for CFD validation for resistance and propulsion thus many experimental and numerical data exist about this geometry. The same model geometry was also used in [19], [27], [35], [37] and

[42].

A complete set of measurements was carried out in a previous work [37] for Froude 0.35 on a model of DDG51 that was 5.720 meters long (INSEAN model C.2340). This Froude number was chosen because the wave formation presented a developed plunging breaker on the bow wave, a large area of breaking and also a relatively steady wave pattern.

With the analysis of the photos of the generated wave patterns relative to model C.2340 it was possible to see that, in the low Froude number range, wave breaking is strongly affected by surface tension. The wave breaking is different from the full scale meaning that information provided by laboratory experiments cannot be extended to full scale. Intermediate Froude number experiments on the 5.720 m hull showed that the model produces a quite steady and well developed breaking and gives a representation of the phenomenon that is more similar to full scale, although still influenced by surface tension. High Froude number experiments would probably represent better the full scale cases, although the realization of their set up is more difficult, mainly due to the high speed and vibration problems. Moreover, the generated waves are not easy to measure, due to the presence of continuous (turbulent) water ejections from the free surface. The same condition of [37], namely Froude number 0.35, was respected for the experiments object of this thesis so to have comparable data.

2.1 Model scale and geometry

Wave breaking is related to the dimensions of the wave, the bigger is the wave the more evident and rich are the dynamics of the breaking. In order to choose the scale λ of the larger model the wave pattern measured for the 5.720 m model was examined. In these measurements the only evident wave system in the field is the divergent wave system. The transversal wave system is mostly cancelled by the wake of the ship and it is disturbed by the reflection of the divergent waves on the side

walls of the basin, thus can not be measured. The model utilized for the test was 5.720 meters long and was towed at a speed corresponding to a value of the Froude number of 0.35. From the measured wave field wave profiles were extracted in direction orthogonal to the shoulder wave crest (see figure 8). These profiles were plotted and the distance between maximum and minimum elevation calculated (figure 9). The average value was used as an estimation of the wave length of the transversal wave system generated by the model sailing at Froude number 0.35.

Cuts were extracted from 9 different lines and the calculated wavelength was ranging from 0.43 to 0.67 meters, the average wavelength is 0.56 meters. From this calculation derives that the real ship waves are around 13 meters long. The wavelength for several model scales was calculated. A model of $\lambda = 15$, towed at the same Froude number, would have been 9.47 meters long and its waves would have been 0.92 meters long. Therefore the scale of the model had to be $\lambda = 15$ or less.

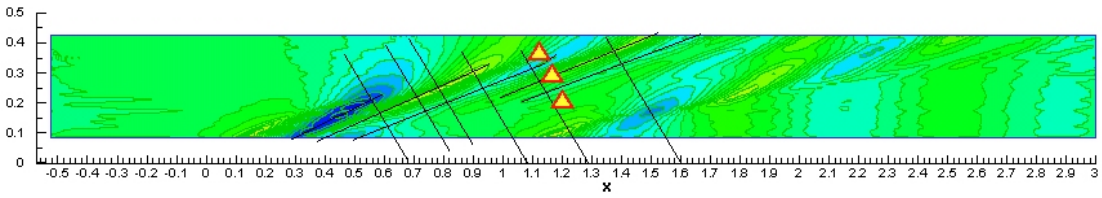

Figure 8: wave pattern measured around a model of $L_{PP} = 5.72\ m$. The lines orthogonal to the crests represent the direction of extraction of the wave profile that can be viewed in figure 9.

The major restrain for the dimensions of the model is related to the laboratory facility. The basin dimensions are to be taken into account relatively to the blockage effect, if the transversal dimensions of the model are too big compared to the transversal dimensions of the basin the model would experience an additional resistance commonly known as blockage effect. Blockage effect can also influence the wave pattern [20], furthermore the basin has to be deep enough for the waves to be considered as deep water waves. To be sure that there is no relevant blockage effect

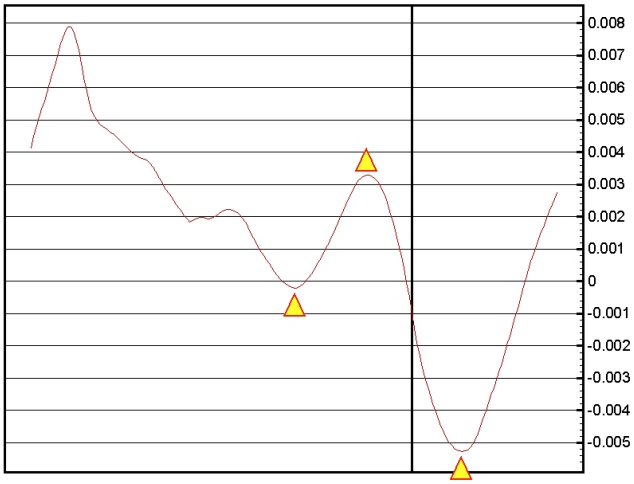

Figure 9: wave profile extracted from the measured wave field, the triangles correspond to the highlighted points in figure 8.

the ratio between the breadth and the width of the main section of the model and the cross section of the channel must be below $1/10th$.

The basin number 1 of INSEAN Institute is 470 meters long with a breath of 13.5 m and 6.5 m deep. The towing carriage is capable of speeds up to 14 m/s and the resolution in the velocity control is 10^{-3} m/s.

From this data follows that the transversal maximum dimension of the model has to be $W_M < 0.1 \cdot W_{Basin} = 1.35$ m. The model scale correspondent to these dimensions would be $\lambda = 14$. The definitive scale of the model is slightly inferior because of the technological constraints relative to the miling machine utilized for model construction. The definitive scale of the model is $\lambda = 14.32$ and the main parameters are listed in figure 1 together with the dimensions of the real ship. The model was named C.2469.

The dimensions of the model thus satisfy the IITC requirements about the blockage

	Real Ship	C.2469
scale	**1**	**14.320**
Lpp	142.00	9.916
Width	18.90	1.320
Draught	6.16	0.430
Displacement	8636.00	2.941
Displacement Volume	8425.40	2.869
Wetted Surface	2949.50	14.383

Table 1: characteristic dimensions of model C.2469 compared with the full scale ship.

effect:

$$\frac{B_{model}}{B_{basin}} = \frac{0.248\ m}{6.5\ m} \simeq 3.8 \cdot 10^{-2} < 10^{-1}, \tag{3}$$

$$\frac{W_{model}}{W_{basin}} = \frac{1.32\ m}{13.5\ m} \simeq 9.7 \cdot 10^{-2} < 10^{-1}, \tag{4}$$

where W_{model} is the maximum width of the model measured at the interception with the water surface and B_{model} is the draught, correspondingly W_{basin} and B_{basin} indicate the transversal and vertical dimensions of the basin.

INSEAN models are built on wood. First the wood planks are glued together. The following step is the numerical miling machine where the model put upside down and is cut symmetrically with two rotative mils. After this step the model's surface does not have the desired finishing yet, thus the carpenters finish the work by hand. Since the miling machine has 5 degrees of freedom some curved parts like the bow bulb cannot be cut by the mils, then are necessarily hand made.

The model was checked section by section with templates, the surface retouched where needed and then painted. After the painting the model dimensions are again controlled and measured with the model upside down on a comparison plane table especially designed for this purpose. At this stage two plane surfaces are prepared, one close to the bow and the other close to the stern of the model. The distance of

Figure 10: first steps of model construction. Left: wood planks are glued together. Right: numerical miling of the bulb.

the upper surface of these planes from the bottom of the hull was measured with accuracy to be used as a reference plane for measuring the draught of the model with the required precision once it is into the water.

The tolerances of the model were under 1 mm.

Turbulence stimulation is obtained trough a line of studs positioned at 60 mm ($\simeq 0.006 L_{PP}$) of distance from the bow, the studs are 3 mm high and are $25 \div 30$ mm far from each other.

The dimensions of C.2469 are out of the standards, thus a special attention was dedicated in reinforcing the model to avoid deformations during the test but also during transportation. The hull thickness was increased and more transversal planks than usual were mounted.

3 Measurement systems, procedures and DREs

Once established the model scale, the test conditions and the areas of interest for the measurements, the design of the test concerns the instrumentation and the measurement procedures. The measurements planned were a photographic study and a resistance test over a range of Froude numbers, the survey of the wave pattern for the established condition of $Fr = 0.35$, mean flow measurements under the breaking waves for the same condition.

The coordinate system that will be used when referring to the measurements is with the x axis directed longitudinally and coincident with the symmetry axis of the ship, y will be the transversal direction positive for the port side and z is the vertical axis positive upwards as shown in figure 11.

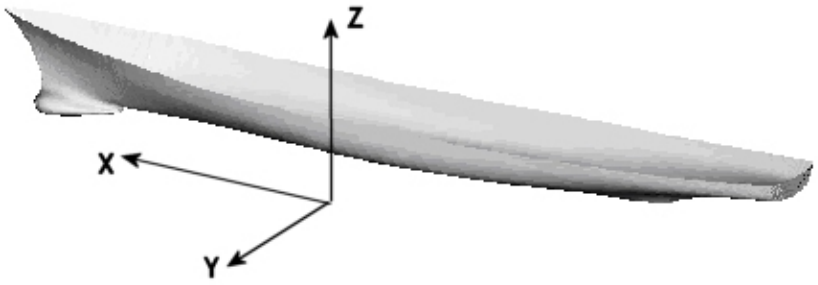

Figure 11: orthogonal system of coordinates adopted for the tests.

3.1 Photographic study

The regions of interest are the bow of the model, in the area where the thin film of liquid fluid climbs the side of the hull and where its front meets the upstream undisturbed water surface, the wake of the bow wave, where the surface can be turbulent, the area of the shoulder wave, the location where the two crests meet.
A photographic camera situated in front of the bow and looking backwards can have a view of the bow, of the location where the bow wave originates, of the recirculation of the bow wave crest and of the evolution that follows the impact of the crest on the water. A side camera looking at forward direction from behind gives a view of the area of the wake of the breaking bow wave and provides a survey of the shoulder wave, with particular attention to the points where the bow wave and the shoulder wave crests cross each other. The aim was to have detailed images of the free surface, at the three model scales, in the same area where the measurements of the wave pattern are planned.
Two digital cameras were utilized with the purpose of obtaining high resolution pictures of the areas of interest. The cameras are two Nikon D100 that can be remotely operated. The pictures where shot with a resolution of 300 dpi in both horizontal and vertical direction with a dimension of 3008×2000 $pixels$, enough to be able to look at the details of the breaking waves. The color of the images is a 24 bit deep and the images have been saved in jpg file format with the lowest compression. The exposure time was set in $1/60th$ of a second and the camera flashlight was used, the diaphragm number was set in 5.6 for all the pictures while the focal length varied to adapt the subject to the frame: since the camera position could not be changed, while the three models are of course of different dimensions. The cameras were installed on the carriage, powered by rechargeable batteries and connected by wire to the control panel. The pictures were shot manually after the clamp that holds the towed model was released, as soon as the test speed was reached.

3.2 Resistance tests

The resistance test were conducted together with the photographic study for Froude ranging from 0.05 to 0.45 and for three different scales of the model.
In July 2004 the three models of the ship were equipped for the towing tank test at INSEAN basins. The tests were scheduled and carried out on the same facility, basin number 1, for all the models so to avoid possible differences due to the change of experimental facility (facility bias).
The standard configuration for towing tank test was used, following the ITTC rules [22] each model was equipped with a load cell, the towing line has to be horizontal and lay on the free surface plane in the advancing direction as schematized in figure 12.

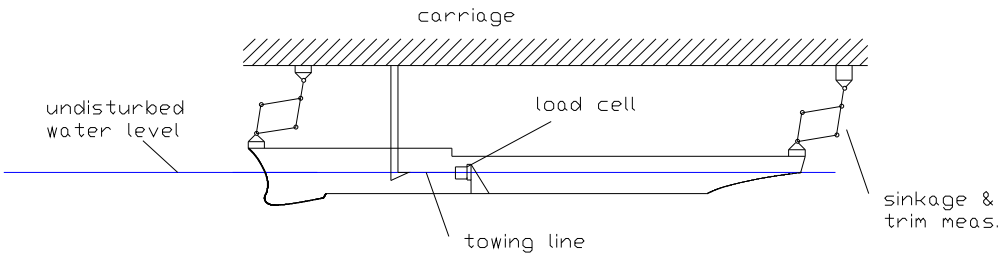

Figure 12: scheme of the constraints of the experimental set-up for drag measurements on a model.

Being the range of resistance values very extended it was necessary to use three different load cells to cover the entire range of resistance forces of the largest model (C.2469), two were needed for the middle scale model (C.2340B) and just one for the shortest (C.2385). When a load cell was changed the last run was repeated with the new cell for having overlapping data with the different set ups.
The characteristics of the load cells can be viewed in table 2, the range is indicated in Newton in the same table.
The load cells are Hottinger Baldwin Messtechnik manufactured in Germany, their

model name	C.2469	C.2340	C.2385
model scale	14.320	24.824	46.588
load cell range [N]			
100			HBM12 F
200		HBM11 F	
500	HBM28 F	HBM28 F	
1000	HBM22 F		
2000	HBM17 F		

Table 2: load cells used for the measurement of drag resistance on the different models.

class of accuracy is 0.2 expressed as percentage on the full range. The cells are calibrated at INSEAN with masses that are regularly checked by a specialized society that refers to Istituto Metrologico Colonnetti of Torino that in Italy has the reference samples. Following the ISO9001:2000 procedure every time an instrument is calibrated a certificate is released reporting the calibration masses used, the characteristics of the instrument, sensibility and offset coefficients and the environmental conditions.

The models were ballasted with lead masses of 10 kg (and fractions for fine adjustments) to the point where they the reached the design displacement condition. The model was ballasted up to the calculated displacement, the difference between the draught obtained in this way and the theoretical one was measured and it was under 1 mm, as expected with the usual accuracy our models are built.

The ballast of the model was calculated following the procedures of ITTC 1978 [21], the real scale ballast can not be simply scaled with the model dimensions but it has to be taken into account that the ship is designed for sailing in sea (salted) water while towing test are performed in fresh water, the ITTC value for the density of sea water is $\rho = 1025\ kg/m^3$ in standard conditions, hence the formula for calculating

the displacement ∇ of a model from the displacement of the full scale ship is:

$$\nabla_{model} = \nabla_{ship}/(\lambda^3 \cdot 1.025), \tag{5}$$

the result is the total displacement of the model. To calculate the ballast needed to reach the displacement the model is weighted together with all the on board instrumentation, this weight is subtracted from the displacement as calculated from 5 to obtain the ballast.

The measurement system for sinkage and trim is a potentiometric device connected to the fore and aft crossbars at bow and stern of the model, on the same locations where the draught of the model is measured. The system is constituted by two weight balanced mechanical parallelograms that are also used to keep the model on a straight run (figure 12).

The ITTC rules for resistance tests state that the direction of the towing force must be horizontal and the model left free to take its own trim and sinkage. The position of the point were the model is towed from can be varied to set exactly the towing direction, its position is evaluated after the model is ballasted up to the sinkage and trim correspondent to zero speed.

The models were tested without any appendage in order to measure the so called *naked resistance* of the models.

The test speed is greater for a bigger model at the same Froude number, in practical terms this means that three different conditions can be tested each run for the smallest model and no more than two for the largest, taking also into account that, being the mass of the large model quite relevant, the accelerations had to be kept as low as possible in order to avoid excessive loads on the structure, thus further decreasing the acquisition time available per run.

In order to avoid continuous progression of the test from the lowest to the fastest speed the testing velocities were alternated from one run to the other. The model was held during the acceleration phase, released when the test speed was reached and the measure taken. Then the model was held again and the carriage accelerated

till the next test velocity was reached and the procedure was repeated till the end of the basin. Lower speeds were tested in the first part of the run because the waves generated by the model have its same speed, if the second part of the run was slower than the first, the waves produced at the fastest velocity would reach the model and spoil the measurement, this means that the testing speeds scheduled for one run should be ordered from the lowest to the fastest.

The temperature of the water was taken twice a day at the immersion of the bottom of the hull's model. Since it was summer time the temperature was not changing at all from early morning till the end of the day. The resistance tests for the three models were all completed in a four days period, this short duration of the test guarantees that laboratory conditions were as similar as possible from one test to the other.

During these tests the following quantities were measured: the model speed, the towing force, the sinkage and the trim of the model and two images where taken each test speed, one for the bow wave and another for the shoulder wave as previously described.

The data reduction equation (DRE) that links the signal given by the load cell to the measured force is:

$$R = K_{force}(V - V_0), \tag{6}$$

this is a simple linear relation that links the voltage V given in output by the instrument to the resistance force R of the model, V_0 is the zero of the load cell. The load cells are utilized in their linear range.

The velocity of the carriage is measured with a system constituted by a tachometric wheel that induces 1000 pulses on an optical encoder for every meter of displacement, thus the spatial resolution is 0.001 m. The pulses are counted by a 16 bits binary device and the velocity of the carriage $v_{carr.}$ is thus given by the following relation:

$$v_{carr.} = \frac{n}{T} \cdot 0.001, \tag{7}$$

with n being the number of pulses counted in the time T.

3.3 Wave elevation tests

The wave elevation pattern around the hull was measured in the near field of the C.2469 model. The tests of wave path measurement and flow field were performed in restrained conditions. This means that the model was not anymore allowed to take its own trim and sinkage but was locked at the position it would naturally take at Froude 0.35 as inferred from the resistance tests. As shown in figure 13 the device for connecting the model to the towing carriage is designed in such a way that the model can be put at the specified sinkage and trim and there locked. The correct sinkage and trim were obtained ballasting the model till the sinkage and trim the model would naturally take at Froude 0.35, locking it into position and, eventually, adjusting the screws to gain a few tenths of millimeter. This experimental set up ensures that the entire run of the carriage is available for measuring from the moment the test speed is reached. With the model firmly locked in position there is no danger that any oscillation of the model can damage the instruments when measuring close to the hull's side.

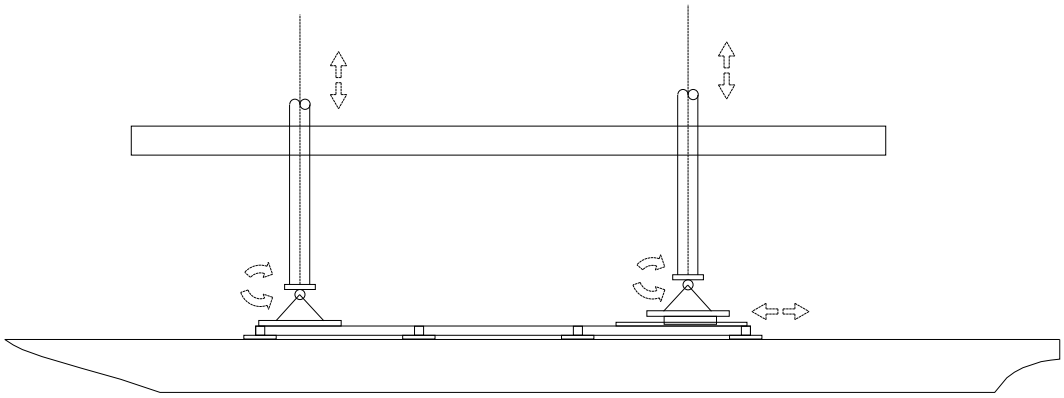

Figure 13: scheme of the constraints of the experimental set-up for wave elevation and flow velocity measurements.

The instrument for the measure of the wave elevation field is a Japanese servo me-

chanic probe built by Kenek, model SHT3-30. This probe has a metallic pin with a very small diameter hence its resolution is around one tenth of a millimeter. The extremity of the pin senses the water searching for the reference tension that is given by an electrode immersed in the same body of fluid.

The probe gives an output ranging between ± 3 *volts*, its accuracy class is 0.1 and can measure water level variations of 300 mm. The frequency response of the probe varies with the wave amplitude due to the inertia of the rod. For very low amplitudes of the measured wave INSEAN tested the probe for frequencies up to $100Hz$. The measuring grids are lines of points with constant longitudinal x coordinate and variable transversal y location. Each one of these grids represents a transversal cut of the wave pattern (figure 14).

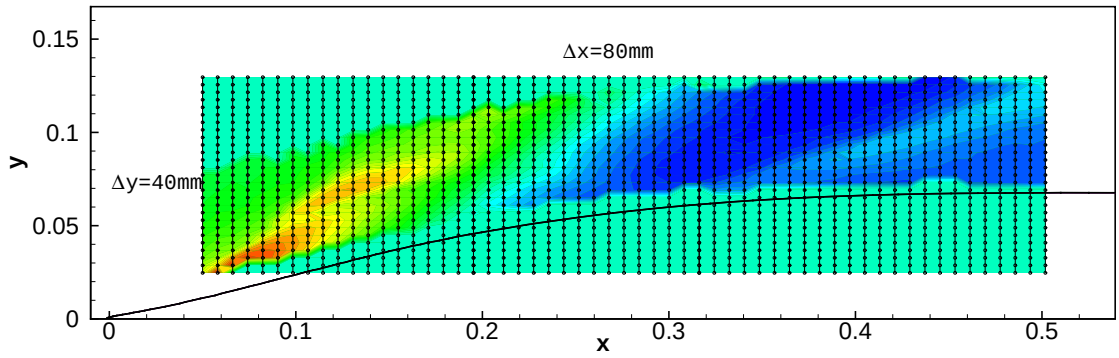

Figure 14: grids for measurement of the wave elevation pattern on C.2469, the black transversal lines are the locations of the measurement transversal sections and the dots are the measuring points. The x and y coordinates are normalized with model length L_{PP}.

The wave elevation pattern was measured point by point displacing the probe in transversal direction at constant x during the run of the carriage.

The longitudinal displacement, the change of x station, was obtained with a traversing system constituted of rectilinear guides and step motor mounted on the towing carriage on the left side of the model, the driving system is a 5 meters long screw,

actuated by the step motor, capable of a resolution of 1 tenth of a millimeter controlled by a Newport digital controller.

On the longitudinal traversing system was mounted the frame carrying the transversal motorized guide driven by a screw connected to step motors for the displacement in y direction, manufactured by Line Tech.

The change in x location was performed once every two runs.

The displacement in y direction was automated in order to acquire several points on one run. The procedure was the following: the control program continuously checked the velocity of the towing carriage. If the speed was constant the acquisition was started at the current location. After the sampling time was passed the program displaced the probe by Δy outward from the hull at the following location and started the acquisition again. When all the points belonging to one transversal section were acquired the probe was displaced backwards by Δx and reset in y towards the hull.

An additional motorized guide of the same type allowed positioning in height (z direction). This possibility was used only at the beginning of the run for the wave elevation measurements in order to position the probe at the correct elevation from the water surface. The resolution of the motors is 200 steps per round and the pitch of the maneuvering screw is 10 mm, meaning that the resulting spatial resolution is 0.05 mm.

The acquisition was done with a PC and an acquisition SCXI system board manufactured by National Instruments connected to the same computer that controls the linear guides.

The inclination of the longitudinal traversing was $\simeq 3/10th$ of degree from the horizontal, being negligible. On the transverse direction the difference between the most internal and the most external point was around 5 millimeters, this difference was acquired every morning on the first section to be measured on the day and treated as the zero value.

Figure 15: transversal and vertical linear guides mounted on the frame for instrument displacement on the hull's side.

The acquisition time per point was set in 8 seconds after the examination of a long time history of the wave elevation at fixed location. The plots of figure 17 are the progressive averages of long time histories from different locations of the wave pattern, sample after sample the average tends to a constant value. The sampling frequency was 1000 Hz. The waiting time between one run and the following was 20 minutes, necessary to restore the conditions in the basin. The next run could not be started until the measured standing wave of the basin was under 1 mm.
To cover the measure area 150 runs of the carriage were needed, the wave elevation field was measured point to point in 1168 locations belonging to 57 transversal sections with a longitudinal step of $\Delta x = 80\, mm$ and a transversal step of $\Delta y = 40\, mm$. The data reduction equation for the wave height h measured with the Kenek probe

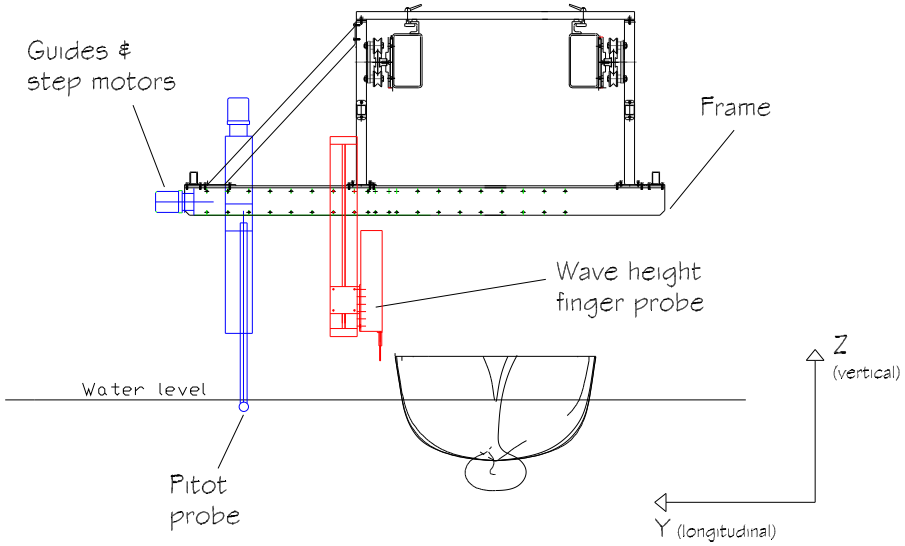

Figure 16: scheme of the experimental set-up and frame for supporting and moving both probes, the wave probe moves only in transversal direction, the Pitot probe moves both in vertical and transversal directions.

and normalized with respect to the model length L_{PP} is:

$$h = \frac{K_{kenek}(e - e_0)}{L_{PP}}, \tag{8}$$

where K_{kenek} is the sensitivity coefficient of the probe as deduced from the calibrations, e is the voltage reading and e_0 is the reference zero voltage.

3.4 Flow velocity tests

The objective of the test was to measure the mean velocity of the flow close the water surface at the locations where breaking phenomena takes place. The data will be used for the evaluation of the influence of the breaking waves on the near field flow. The model was towed at the fixed sinkage and trim for Froude equal to 0.35 with the same set-up illustrated for the wave elevation test.

The velocity was measured by a 5-holes Pitot probe. The head of the probe is shaped to have five faces, each one hosting a hole, the central hole is located on the

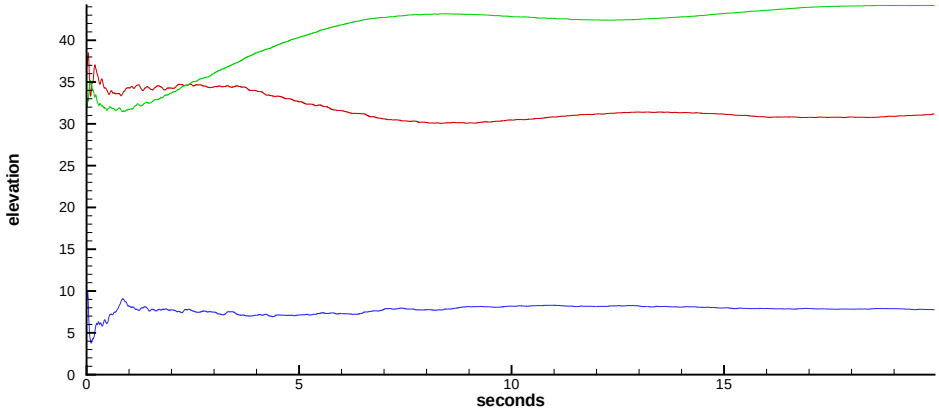

Figure 17: progressive averages of the wave elevation time histories measured in three different locations.

plane oriented perpendicularly to the advancing direction, the upper and lower hole are on the faces oriented at 45 degrees above and under the central one, so are the left and right hole on the respective faces. Built in this way the probe is capable to acquire five different pressure signals and from these signals, through the data reduction algorithm and the calibration maps, it is possible to calculate the three different components of the velocity vector at the measuring location. The head of this Pitot has a diameter of 5 millimeters, this determines the maximum resolution of the instrument.

The Pitot probe was built at IIHR and there calibrated by INSEAN engineers at the wind tunnel to obtain the calibration maps.

The pressure signal is sensed by 5 differential pressure transducers built by Validyne model DP15 that can mount different laminas to adapt their sensibility to different situations. The measuring range of the laminas had to be greater then the maximum expected pressure that can be simply calculated:

$$p_{max} = \frac{1}{2}\rho v^2 \simeq 6000\ Pa, \tag{9}$$

where $v = 3.452\ m/s$ is the test velocity correspondent to $Fr = 0.35$ for the large model, $\rho = 1000$ is the density of the water.

The transducers were calibrated with a Ametek pressure balance model PK 654 that works with reference masses and that is regularly checked by the calibration Institute in analogy with the case of the load cells previously described. The five

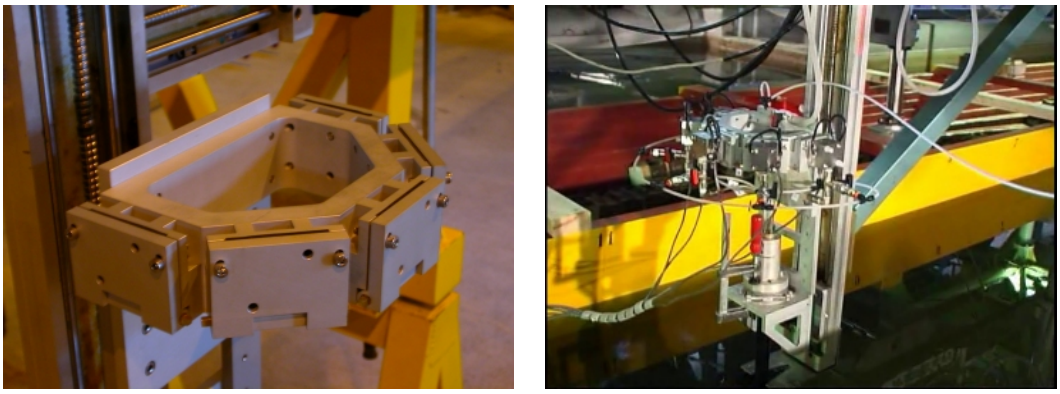

Figure 18: left, support for the group of 5 differential pressure transducers on the vertical guide. Right, the transducers and the hydraulic circuit are mounted on the support above the Pitot on the hull's side and ready to go.

holes of the Pitot are each of them in connection with one side of a differential pressure transducer. The other side of the five pressure transducers is connected to the reference pressure that is the same for all of them. This reference pressure is taken from another Pitot probe, immersed in the undisturbed flux in front of the model and far enough not to disturb the water of the basin before the passage of the model.

The five pressures from the 5-holes Pitot probe are the dynamic components of the total pressure. The static component is taken from the other Pitot. In this way the five pressures are calculated as the differences between the dynamic pressures taken by the 5-holes Pitot probe and the reference pressure that was the same for all. Once the pressure signal is acquired the data reduction equations were used to calculate the intensity and direction of the velocity vector using the calibration

maps relative to the 5-holes Pitot probe.

As for the wave pattern also the mean velocity flow is a point wise measurement. Thus the procedure was similar: the probe reached a certain position inside a grid of points, acquired the signal for the specified time, then was moved to the following location and started again till the end of the rectilinear basin was reached and the towing carriage began to slow down. The grid for the wave elevation measurement was a line of points at constant x and the probe was moving in positive y direction. The grid for the mean flow velocity measurements was the immersed part of a transversal xy plane at constant x. The probe was displaced automatically by the computer during the run first in y direction and then, when an horizontal line of points was acquired, in z direction for changing line on the grid. The device for the vertical displacements was a rectilinear guide identical to the one used for horizontal displacements and described for the wave pattern measurements.

The elaboration program was capable to analyze the signal taken on the carriage way back thus giving a precious indication if it was the case to repeat the acquisition because something went wrong. It could happen, for instance, that some air or particle of dirt of the basin water remained inside the Pitot tube pipes spoiling the measure. Before every run this possibility was checked by going trough a *zeroing procedure*: the Pitot's head was lift close to the water surface and the zero signal was acquired, then the probe was driven down at maximum depth and the zero value was again checked, these two values had to be the same because the pressure does not depend on the depth of the probe. If this was not happening it meant that one of the pipes of the Pitot was obstructed. With the same procedure it was possible to check if there was some air in the Pitot circuit, actually, if some air is caught in the pipes, it will be compressed when the depth of immersion of the probe increases, this would result in a change of the signal pressure in the transducer.

Every time it was necessary the hydraulic circuit of the Pitot was cleaned with distilled water that was let run trough the transducers down to the Pitot pipes and

finally flowing through the head holes pushing out the air bubbles, in this way the Pitot probe and the transducers were always filled with distilled water avoiding the risk of formation of calcareous obstructions inside probe.

The next run was started after the waiting time for the water of the basin to calm down, this time was set in 15 minutes and the state of the basin was checked with the wave elevation probe. In order to consider the water surface as calm the level variation of the water surface had to be less than 1 millimeter.

The acquisition time was set in 5 seconds with a sampling rate of 100 Hz, two different spacing of the grids were utilized $\Delta z = \Delta y = 24.79\ mm$ corresponding to $0.0025 L_{PP}$ and $\Delta z = \Delta y = 12.40\ mm$ $(= 0.00125 L_{PP})$.

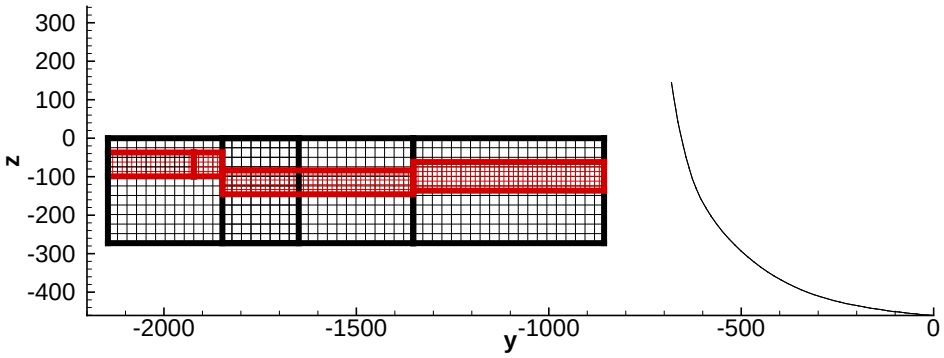

Figure 19: measurement grids for the mean flow velocity on section 0.40 of C.2469. The black grids are spaced $0.0025 L_{PP}$ and the red grids are refined (step size $0.00125 L_{PP}$). The x and y coordinates are normalized with model length L_{PP}.

The horizontal span of the rectilinear guide of the Pitot was not enough extended to cover the entire measurement area. This difficulty was resolved by varying the relative position, namely the transversal distance, between the hull and the frame supporting the probe. The final measured grid will be thus the result of the union of several grids as shown in figure 19.

In figure 20 the most internal measurement grid relative to section 0.35 is shown together with the correspondent wave elevation line as deduced from the measure-

ments. All the points that will not be occupied by the water were excluded from the path of the Pitot's head. This procedure allowed to save running time of the carriage and minimized the risk of air bubbles being entrapped in the Pitot's holes. The three components of the mean velocity vector relative to each point location, as

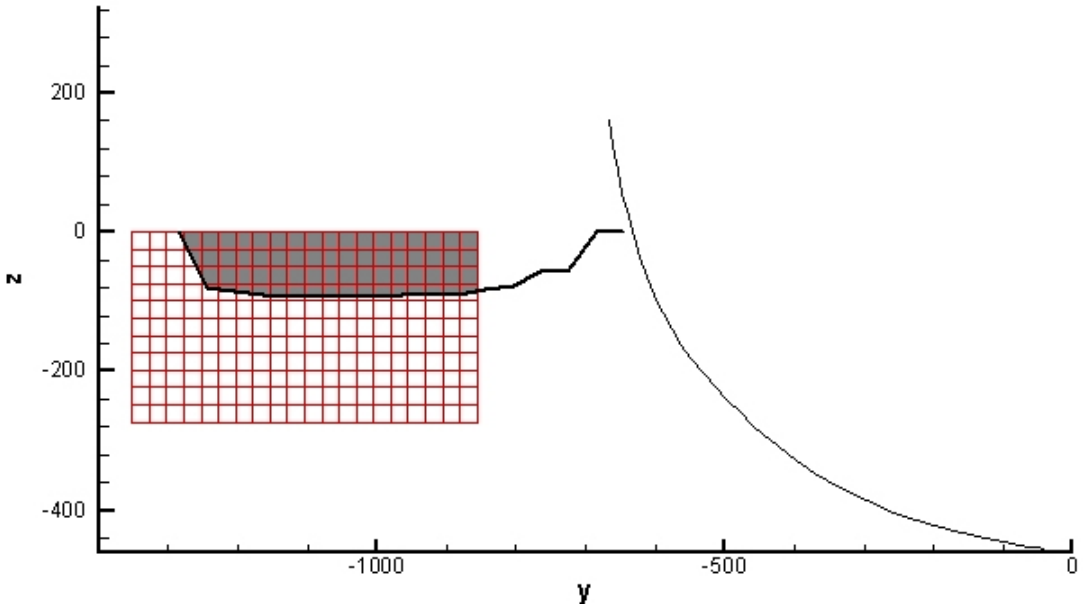

Figure 20: section 0.35, the measurement grid is partially out of the water, the grey area represents the points that will be excluded from the measurement.

well as the pressure coefficient C_p, were calculated from the measured data of pressure on the 5 holes of the Pitot probe using the following data reduction equations (DRE):

$$u(x,y,z) = (VX\cos\alpha_p\cos\phi_p + VY\sin\phi_p + VZ\sin\alpha_p\cos\phi_p)/U_c, \tag{10}$$

$$v(x,y,z) = (-VX\cos\alpha_p\sin\phi_p + VY\cos\phi_p - VZ\sin\alpha_p\sin\phi_p)/U_c, \tag{11}$$

$$w(x,y,z) = (VZ\cos\alpha_p - VX\sin\alpha_p)/U_c, \tag{12}$$

$$C_p(x,y,z) = \frac{2(p-p_0)}{\rho U_c^2} = \frac{2H_c' - \rho PV'^2}{\rho U_c^2}, \tag{13}$$

where,

$$VX = V' \cos\phi \cos\alpha, \tag{14}$$

$$VY = V' \sin\phi \tag{15}$$

$$VZ = V' \cos\phi \sin\alpha, \tag{16}$$

$$V' = \sqrt{\frac{2M'}{\rho M}}, \tag{17}$$

$$M' = 4H'_c - H'_t - H'_b - H'_p - H'_s, \tag{18}$$

$$K' = \frac{H'_t - H'_b}{4H'_c - H'_t - H'_b - H'_p - H'_s}, \tag{19}$$

$$L' = \frac{H'_s - H'_p}{4H'_c - H'_t - H'_b - H'_p - H'_s}, \tag{20}$$

in these equations α_p and ϕ_p are the 5-holes Pitot probe preset angles of pitch and yaw and α and ϕ are thee measured pitch and yaw angle of the velocity vector in the coordinates of the probe; H'_i (where $i = c, t, b, p, s$) are the measured pressures for the center, top, bottom, port and starboard holes respectively. The reference pressure is p_0 taken from the side holes pressure of the static Pitot probe.

The primed variables designate the local measured values and the coefficients computed using this values, whereas the unprimed variables $K,\ L,\ M, P$ are the variables that come from the wind tunnel calibration of the Pitot. α and ϕ are obtained from K', L' and their corresponding 5-hole Pitot probe calibration coefficients ($K,\ L$) and they are used to obtain the values of M and P.

4 Froude numbers and scale effects

Three models of three different scales have been towed in the rectilinear basins in a wide range of Froude numbers. Their dimensions and scales are reported in table 3. The models were set up for the resistance test, thus they were free to take their own sinkage and trim and obliged to keep a rectilinear route. During these tests pictures of the wave pattern were taken at each speed for every model and will be shown and discussed in the first paragraph of this chapter. Then the results of the resistance measurements will be presented. The same methodology described in [37] will be

	Real Ship	C.2469	C.2340	C.2385
scale	**1**	**14.320**	**24.824**	**46.588**
Lpp [m]	142.00	9.916	5.720	3.048
Width [m]	18.90	1.320	0.761	0.406
Draught [m]	6.16	0.430	0.248	0.132
Displacement [Kg x 1000]	8636	2.941	0.565	0.085
Displacement Volume [m^3]	8425.40	2.869	0.551	0.083
Wetted Surface [m^2]	2949.50	14.383	4.786	1.359

Table 3: resume of the main geometrical parameters of the models.

here adopted.

4.1 Photo study

As described in chapter 2 two cameras were utilized during the resistance tests for taking pictures of the area of the bow wave and its wake and of the shoulder wave.

Due to the great difference in the dimensions of the models it was not possible to have the same orientation for the three scales on the shoulder wave picts, thus the perspective is different. The layout of the figures (figures from 34 to 42) is the same for all the conditions: from top to bottom the front and the back view of the models of C.2385, C.2340 and C.2469 are shown on the same row. The lengths of the models and the velocities corresponding to the different Froude numbers of test are reported in table 4.

	C.2469	C.2340	C.2385
Lenght [m]	9.916	5.720	3.048
Froude number	test speed [m/s]		
0.05	0.493	0.374	0.273
0.1	0.986	0.749	0.547
0.15	1.479	1.123	0.820
0.2	1.972	1.498	1.093
0.28	2.761	2.097	1.531
0.3	2.958	2.247	1.640
0.35	3.451	2.621	1.913
0.41	4.042	3.070	2.241

Table 4: test velocities for the three model scales.

In order to highlight the visual observations enlarged pictures will be presented when necessary. The description will be done from the lowest to the highest test velocity. For $Fr = 0.05$ the water surface is barely disturbed by the passage of the model, its appearance is smooth for the two smaller scales, only the crests of the bow wave system of the model C.2469 are visible in figure 34 bottom left. The flow is laminar and there is no transition to turbulence at the solid wall of the hull.

At Froude 0.10 the wave crests are visible at the three scales. In the case of C.2469 the bow wave begins to form and to show a mild spilling breaker completely absent for C.2385 at this Froude. A slight turbulent perturbation of the free surface is visible only very close to the hull of the larger model indicating the beginning of the separation (see figure 21). While the surface is still very smooth on the other

two scales. In the back view many crests are visible on the models' side due to the still low velocity, their number will decrease as Froude increases because of the dispersion properties of water waves.

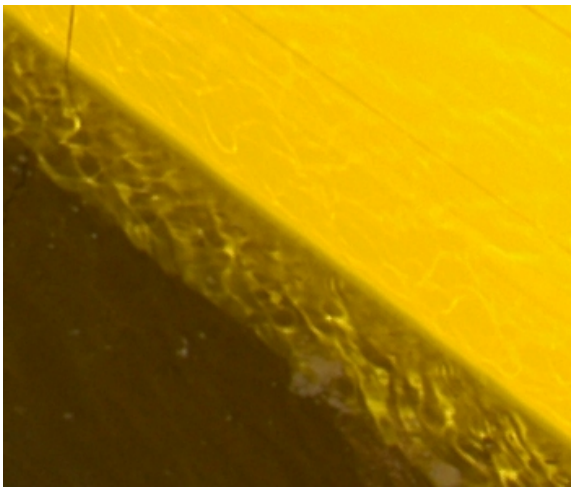

Figure 21: enlarged particular of the flow close to the C.2469. The first index of free surface turbulence appears on the boundary of the larger model at $Fr = 0.10$.

For the velocity correspondent to Froude 0.15 free surface turbulence is already visible at the three scales. In the pictures relative to C.2340 the first three wave crests are very clear. The mild breaking that was already visible at $Fr = 0.10$ is now extended more far from the hull on the wave crest, comparing the first two images of figure 22 this is evident. The area behind the crests, the wake of the waves, begins to be perturbed by breaking. C.2469 shows surface perturbations close to the hull and behind the bow wave crest more extended then for smaller scales.
At $Fr = 0.20$ on C.2340 and C.2469 the breaking interests not only the part of the crest immediately close to the bow of the model but it is extended farer from the hull (see again figure 22). The bow wave of the larger model begins to show the first indication of a scar that will become more evident for higher Froude numbers. An enlargement of the bow wave crest (figure 23) shows the beginning of a scar as a consequence of the impact of the bow wave onto the underlying water. Indeed, the

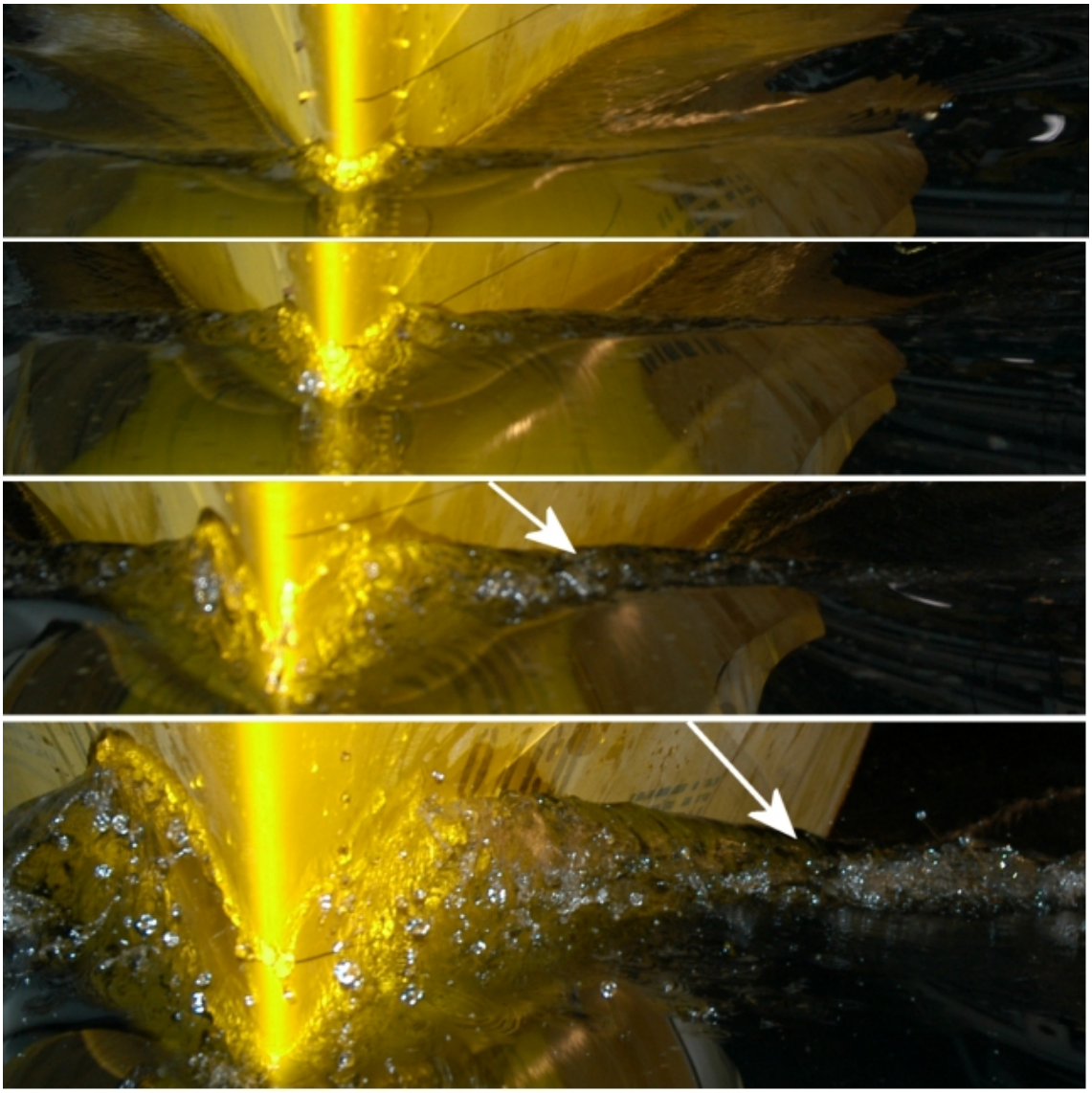

Figure 22: the bow wave crest of the model C.2469 at Fr=0.10, 0.15, 0.20 and 0.28, the arrow highlights the location of the scar produced by the splash up visible also in the following figure 23.

wave crest has probably enough energy at this scale to begin to splash up. Also the form of the crest differs between C.2340 and C.2469. The crests of the first waves make an angle with the advancing direction that decreases when following the crest line away from the hull, this can be see in figure 37 back view and in the enlargement of figure 24. The crests of the other waves are straight lines with constant angle

with the advancing direction, furthermore the wake of the bow wave begins to be sensibly under the undisturbed water level.

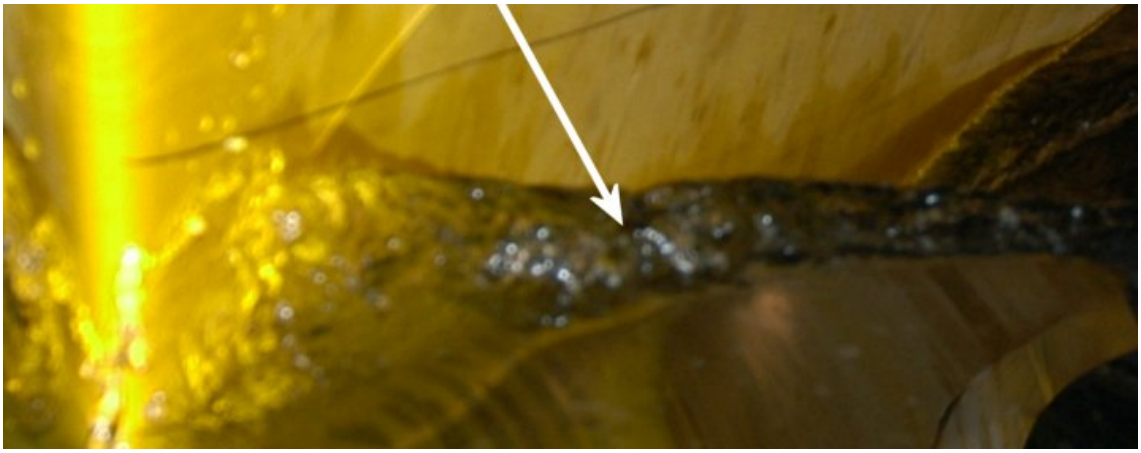

Figure 23: the bow wave crest of the model C.2469 at Fr=0.20 begins to show a splash up scar.

At $Fr = 0.28$ (figure 38) the scale begins to show its influence. As observed in [37] the small model bow wave changes behavior from non breaking to breaking state but without overturning of the crest as the wave dynamic is still mainly influenced by surface tension. On the other side, the bow wave breaking is very different for the large model if compared to the other two (figure 22 bottom picture). The bow wave is still in spilling breaking conditions for the small and the middle model (figure 38). The crest of the wave has the appearance of a smooth roll on C.2385, seems to be more energetic on the C.2340. On C.2469 the bow wave displays a marked change in the behavior of the crest before and after the maximum wave elevation point (figure 25). Before the maximum is reached the crest looks like a bore advancing upwards on the side of the hull, the gravity force counteracts its inertia and from its front several water drops are ejected forward. After the maximum height is reached the whole front curves downwards under the action of gravity and creates a large tunnel under the uppermost layer of the water free surface. This layer bents down under the action of gravity and eventually impacts the undisturbed water surface.

Figure 24: the line crest forms an angle with the advancing direction that varies for the first two waves when moving away form the hull at $Fr = 0.20$.

The bottom line of figure 38 shows that the wake of the bow wave is still quite smooth for the C.2385 and more perturbed on the C.2340. The crest line of the first wave bents backwards and crosses the crest of the trailing waves behind it. On the picture relative to C.2469 some air bubbles are visible on the surface, probably air entrapped under the bow wave crest and emerging downstream. The shoulder wave crest begins to straighten close to the hull. In the figure 38, central row, relative to C.2340, the shoulder wave is in breaking conditions on wide portion of its crest, more extended breaking on this crest is visible on the larger model while no breaking at all is present for the small C.2385. This scale still shows a capillary wave train riding in front of the non breaking shoulder wave crest, see figure 26.
At $Fr = 0.30$ (pictures of figure 39) the conditions are very similar to $Fr = 0.28$. The scale effects begin to be evident also between the scales of C.2340 and C.2485

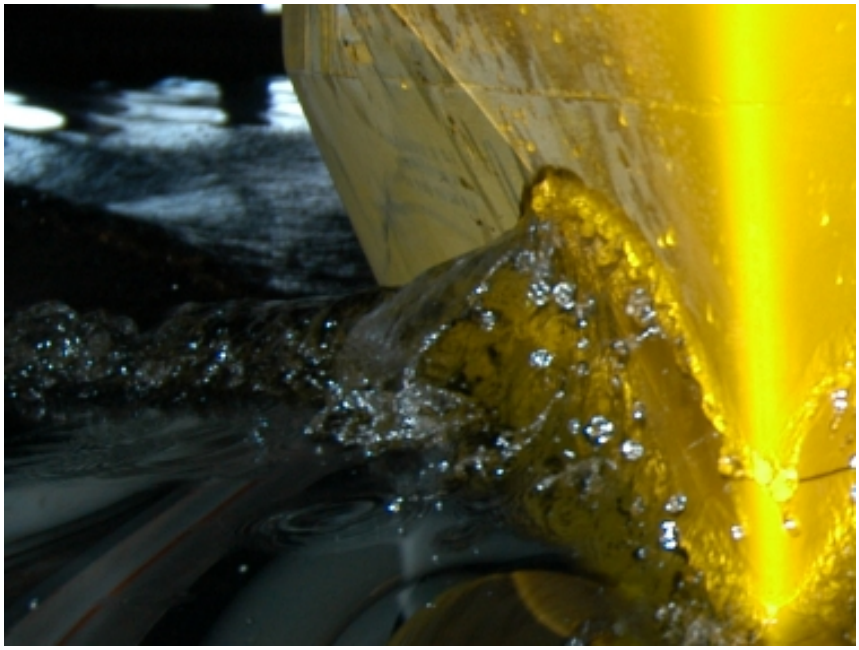

Figure 25: particular of the bow wave of C.2469 at $Fr = 0.28$. The first part of the wave is characterized by the formation of drops whereas in the second part the water on the crest turns over and falls down.

and the differences may be observed looking at the shoulder wave breaking. [37] reports that, at this Froude number, several details that were damped by surface tension begin to emerge at both the small and the middle scale. The scale effect on the bow wave is now more evident between C.2340 and C.2469: on C.2340 the beginning of overturning motion of the bow wave crest is clearly visible but there is still no evidence of water ejection from the crest. While this happens for C.2469 where the wave front is completely ragged like was already for Froude 0.20 at this scale. From the bottom picture of figure 39 the crest of the bow wave can be seen behaving like a developed plunging near the bow of the model. Following the crest, farer from the hull, the same wave has a spilling like behavior.

The breaking of the bow wave is different from the one relative to the shoulder wave were no plunging occurs even close to the hull. The shoulder wave, when breaking, is always in spilling breaking conditions.

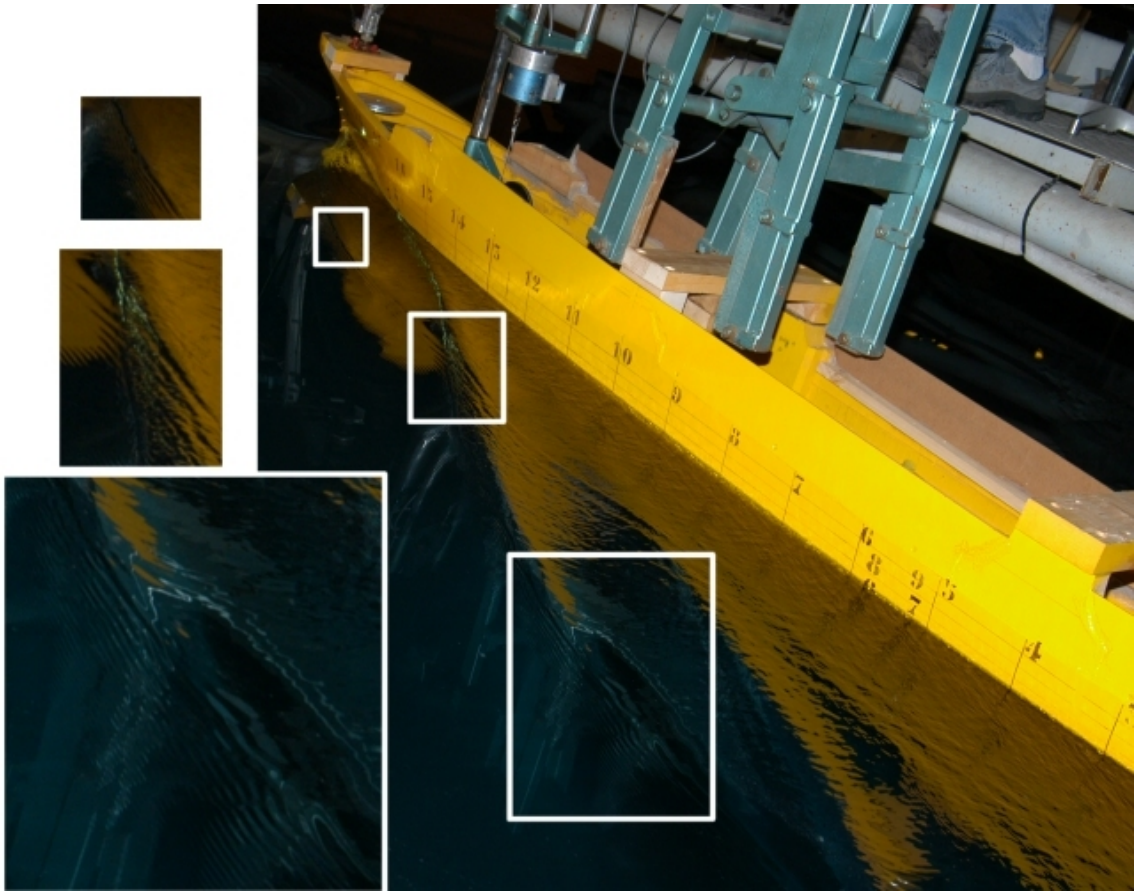

Figure 26: wave pattern of C.2385 at conditions relative to $Fr = 0.28$, at this model scale the capillary wave trains are still visible in front of the bow and shoulder wave crests.

When looking from behind, the scars generated by the secondary splash up begin to be visible on the wake of the bow wave for C.2340 scale, but are dissipated before they reach the shoulder wave front, see the enlargement of figure 27. These scars on the water surface are not seen on C.2385 at this speed yet.

At $Fr = 0.35$ (figure 40) the shoulder wave crest is definitely a straight line at all the scales, whereas the breaking on the three models is completely different. The wake of the bow wave of the smaller model is turbulent (figure 40 top row) while the middle model has both crests in breaking conditions with air entrapped in the form of white water congruently with previous observations reported in [37]. The

Figure 27: wave pattern of C.2340 at $Fr = 0.30$. The bow wave breaking begins clearly to show in its wake the scars generated by the splash up of the crest.

wave fronts on the smaller scale models are still regular lines, the scars begin to be visible on the bow wave wake of C.2385 (figure 40 bottom left) like it was for Froude 0.30 on the middle scale. Over turning of the bow wave crest of C.2340 (top center picture of figure 40) is more developed but still no significant quantity of air can be entrapped underneath, the scars from the bow wave reach the shoulder wave crest. The large model bow wave ejects water all along its crest that is completely broken, big splash ups of the crest generate two evident scars visible on figure 40 and better highlighted in the figure 28 where the color curves have been modified to put the wave in evidence. In [37] was reported that the wave breaking scenario for the middle model *qualitatively resembles the full scale*, appears here evident, also recalling the full scale images shown in that paper, that the large model pushes this resemblance even further.

At Froude 0.41 the crest of the bow wave of the middle scale model C.2340 is turning over evidently. The scars on the wake are filled with white air bubbles and the first secondary splash up is visible on the front picture (center row of figure 41). The

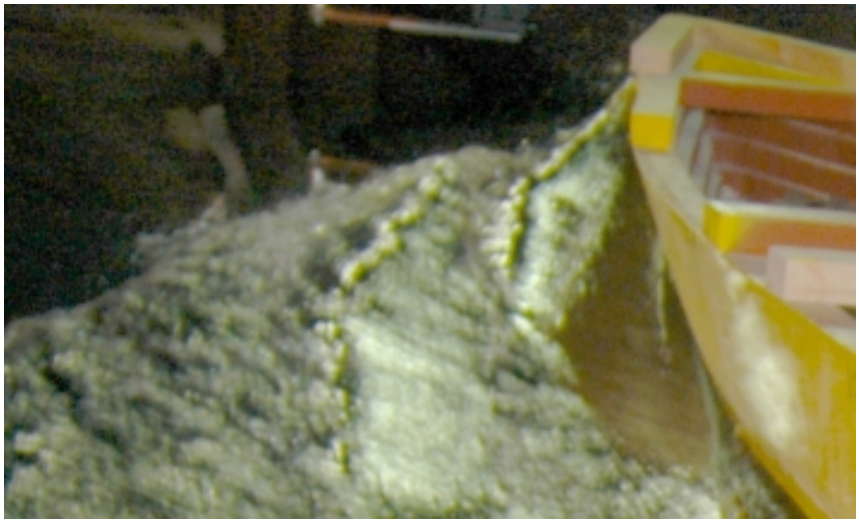

Figure 28: scars from the splash up of the bow wave of C.2469 sailing at $Fr = 0.35$. When model dimensions increase the scars are more definite.

wave pattern of the smaller model is still quite regular (figure 41 first row). Its bow wave is overturning with no significant air entrapment, far enough from the hull the crest line is still smooth and capillary wave crests are still visible parallel to the bow wave crest line, exactly as it was for $Fr = 0.28$ (figure 26), indicating that the breaking did not change too much with the Froude parameter like it has been for the two larger scales. In fact, for the two larger models, the capillary crests are completely cancelled by the principal breaking front and the scars are as visible as the shoulder wave crest is. Also many air bubbles are emerging inside the wake of the bow wave. From the enlarged pictures of figure 29 it is visible the secondary splash up relative to the bow wave of C.2340 and the the generation of the scar.
Froude 0.45 is a limiting condition for the larger scale, in figure 42 top right the bow wave reaches a higher altitude if compared with the C.2340. The splash ups and water ejections are massive on both the C.2340 and C.2469 models. The wave crests are fully breaking with white water all along their visible length while this is not the case for the small C.2385. Due to the smaller length and overall dimension of the waves produced by this model the crest do not brake. There is a small secondary

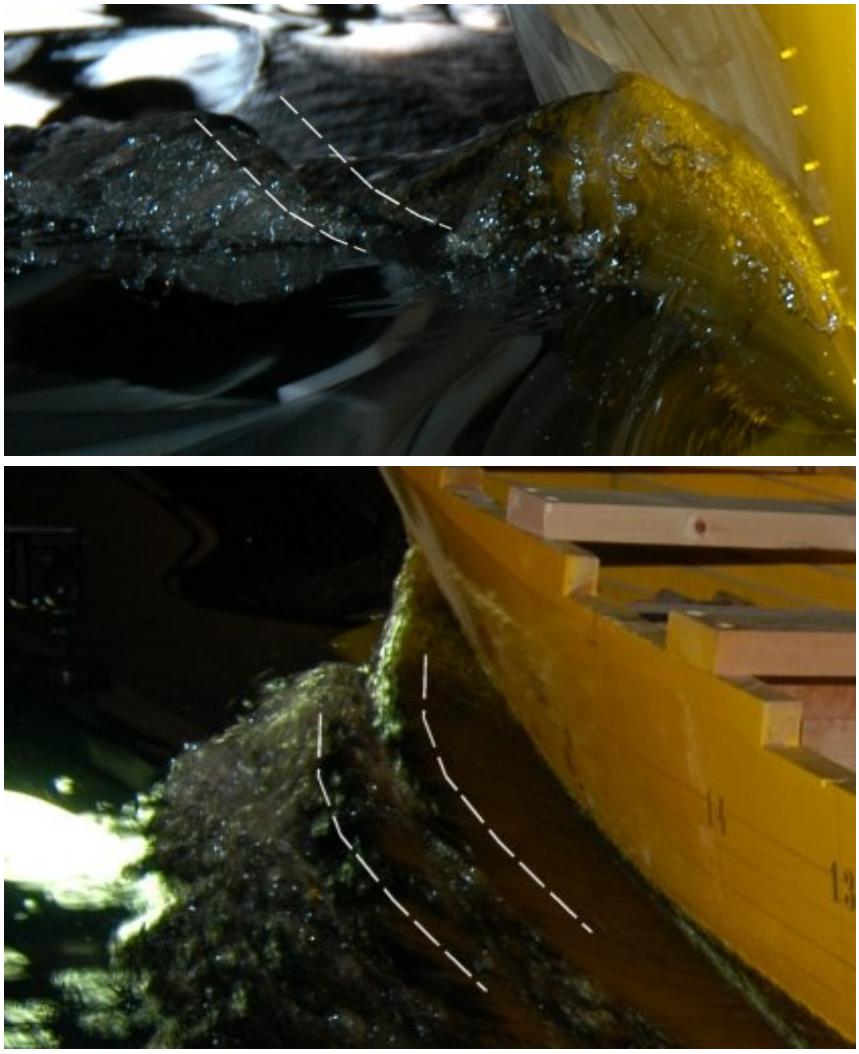

Figure 29: particular of the bow wave of C.2340 at $Fr = 0.41$. The secondary splash up is very evident, the scar generated by this splash up is visible in the bottom image.

splash up of the bow wave but the breaking is very soon dissipated by viscosity and capillary wave crests are always visible in front of the bow wave crest.

The great differences in the wave breaking modality between the different model scales, even at this high Froude number, is exemplar of the scale effects control the near field dynamics.

4.2 Resistance test results

The resistance force to the towing was measured for velocities corresponding to a range of Froude numbers that goes form 0.05 to 0.45. Particular care was dedicated to $Fr = 0.28$ the design velocity, $Fr = 0.35$, the condition chosen for comparison between the different scales, and $Fr = 0.41$, the so called flank speed. For each of these three conditions ten repeated runs were carried out. The data will be utilized for uncertainty assessment.

The test conditions are the same as resumed in table 4.

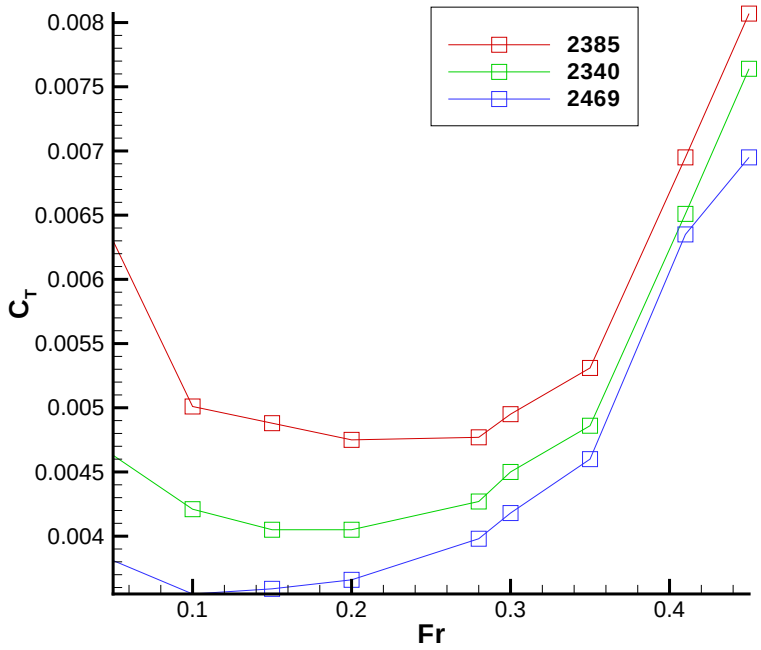

Figure 30: total resistance coefficient C_T measured for the three model scales over the range of Froude numbers.

In figure 30 the plots of the total resistance coefficient are shown. C_R is calculated from the measured total resistance force R_T:

$$C_T = \frac{R_T}{\frac{1}{2}\rho v^2 S}, \tag{21}$$

here S is the wetted surface. The plot of the differences among the models' resistance puts in evidence the relevance of the scale effect. It was already put in evidence in the resistance tests reported in [37], that the resistance force relative to models of different scale changes behavior at different Froude numbers. The results from the resistance tests here reported confirm this trend with the addition of the measurements relative to an even larger model.

As expected the total resistance coefficient has a higher value for the lower scale models for all the Froude range of test. Under some hypotheses proposed by Froude in 1868 the total resistance can be split in two components: a part ascribable to the viscous and inertial forces called frictional resistance and another, relative to gravitational and inertial forces, called residuary resistance.

Following the recommendations of ITTC 1978 and ITTC 1957 [22] the frictional resistance coefficient C_F and the residual resistance coefficient C_R can be calculated as follows:

$$C_F = \frac{0.075}{(\log Re - 2)^2}, \tag{22}$$

$$C_R = C_T - C_F(1 + k). \tag{23}$$

The equation 22 calculates the frictional coefficient of and *equivalent flat plate* having the same surface extension as the wetted surface of the model.

The k of equation 23 is the form factor, a coefficient that takes into consideration the fact that the tangential force on the ship is replaced by the tangential force on a flat plate with the same waterline length and the same wetted surface area as the ship.

The form factor k for this ship takes the value of 0.12, its value comes from the experiments of Longo et al. on a similar model [27] and it is calculated, following Prohaska's method, from low Froude numbers resistance measurements. The Reynolds number is calculated as:

$$Re = \frac{v \cdot L_{PP}}{\nu}, \tag{24}$$

ν is the kinematic viscosity here considered with the value of $10^{-6}\ m^2/s$.

In general the greater part of the residuary resistance for a merchant ship is due to the wavemaking resistance [20].

In figure 31 the residual resistance coefficient is plotted for the three scales. For low Froude numbers the plot relative to the smaller model C.2385 is higher than the other two. The plot relative to the larger model C.2469 starts with the lowest values and, as Froude increases, overtakes first the curve relative to C.2340 at $Fr \simeq 0.18$ and then the plot relative to C.2385 at $Fr \simeq 0.24$. At $Fr \simeq 0.26$ the C_R of C.2340 becomes equal to the smaller model. To put this fact in evidence the difference of the plots of C.2340 and C.2469 with respect to C.2385 is also plotted on the right axis. Part of this difference can be addressed to the different breaking behavior for the three scales. At low speeds, when the flow is mainly dominated by low Reynolds

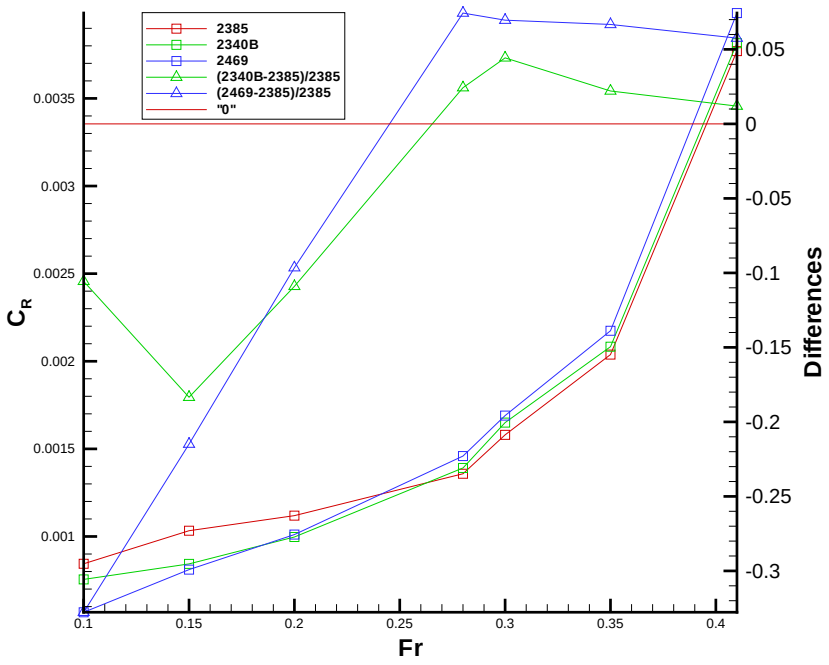

Figure 31: residual resistance coefficient C_R for the three models (left axis). Offset relative to the values of C.2385 (right axis) calculated as $\frac{C_{R(C.2340)} - C_{R(C.2385)}}{C_{R(C.2385)}}$ and $\frac{C_{R(C.2469)} - C_{R(C.2385)}}{C_{R(C.2385)}}$.

effects, the smaller scale experiences a higher specific residuary resistance, but, when breaking appears on the crest of the waves of the two larger models, their resistance increases and overtakes the value of the small ones (the large model C.2469 first, then the C.2340) where breaking is more limited as it has been shown in the photographic study.

In figure 32 the three coefficients are shown together, this plot shows more clearly that for low Froude numbers the resistance of the models is mainly constituted by frictional resistance due to the predominant low Reynolds regime of the flow around the hull. Then, as the Froude number increases, the residuary component of the resistance becomes predominant. The first value relative to C.2385, the shortest of the models, has a different trend but can be excluded from the plot because at this very low velocity (0.273 m/s) the measure becomes difficult due to the oscillations of the towed model. In fact when test velocities are very low (this happens for small models at low Froude numbers) the model resistance is low and does not damp the forward backward oscillation that starts when the clamp is released. To prevent this, very often an additional resistance force is added for damping the oscillations of the model. This was not done in the present case in order to keep the set up as similar as possible for the three scales. Also the higher value relative to the larger C.2469 cannot be considered absolutely reliable, from the bow pictures relative to that condition, figure 42, it is possible to see that the bow wave goes over the bow of the model, thus the model is not is the same conditions of the other two. This happens because the bow of the larger model has been cut as low as possible for it was too high for the towing carriage dimensions. Then the part of hull that was not wet at Froude 0.35 was cut away. At Froude 0.41 the bow wave still does not reach the upper limit of the hull but it does at Froude 0.45 thus spoiling the measurements.

If we exclude these two points the plots of the different models show a common trend.

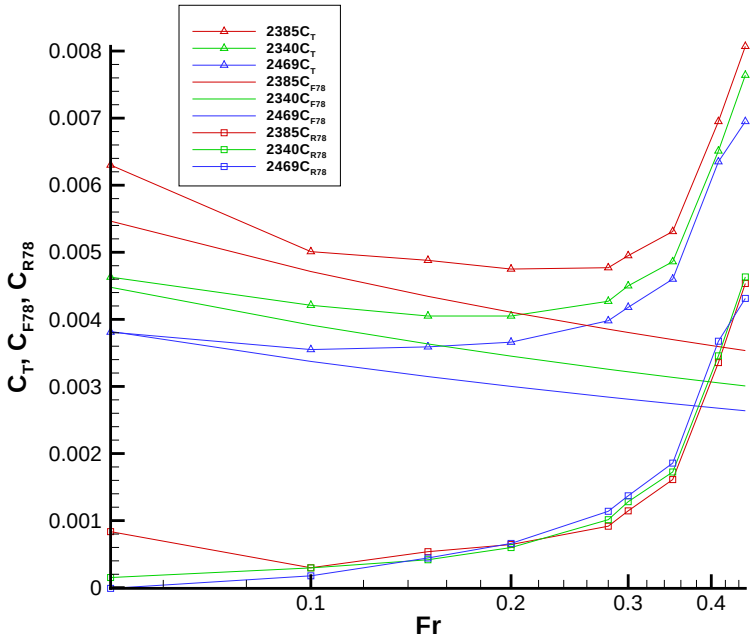

Figure 32: normalized resistance coefficients Cr,Ct,Cf plotted against Froude number.

Finally, the resistance coefficients can be plotted also against the Reynolds number. In figure 33, C_T, C_F and C_R are shown together. This plot shows the different viscous regime in which the models were tested in order to respect the Froude law of similarity of the wave patterns, and puts in evidence the difference between the three scales relative to an integral property like the resistance.

When the resistance component, which depends on the Reynolds number, is subtracted, the residuary resistance contains also the contribution due to the wave breaking. As it is evident by the pictures shown in the figures of section 4.3 the wave breaking is more important at higher Froude number and more intense at larger scales, and it is for the higher Froude number conditions that the value of the residual resistance coefficient of the large model becomes greater then the others giving quantitative evidence of the importance of the scale effect on breaking.

Furthermore the photo study puts in evidence that differences between the flow

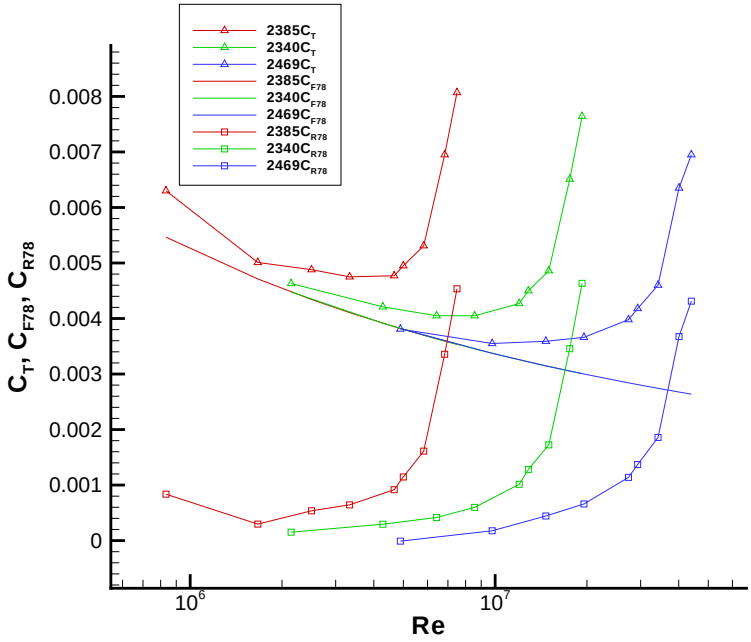

Figure 33: normalized resistance coefficients Cr,Ct,Cf plotted against Reynolds number.

around the models increase at large Froude numbers, consistently with this, also those surface characteristics such as the scars are much more pronounced at large scales.

4.3 Pictures from the photographic study

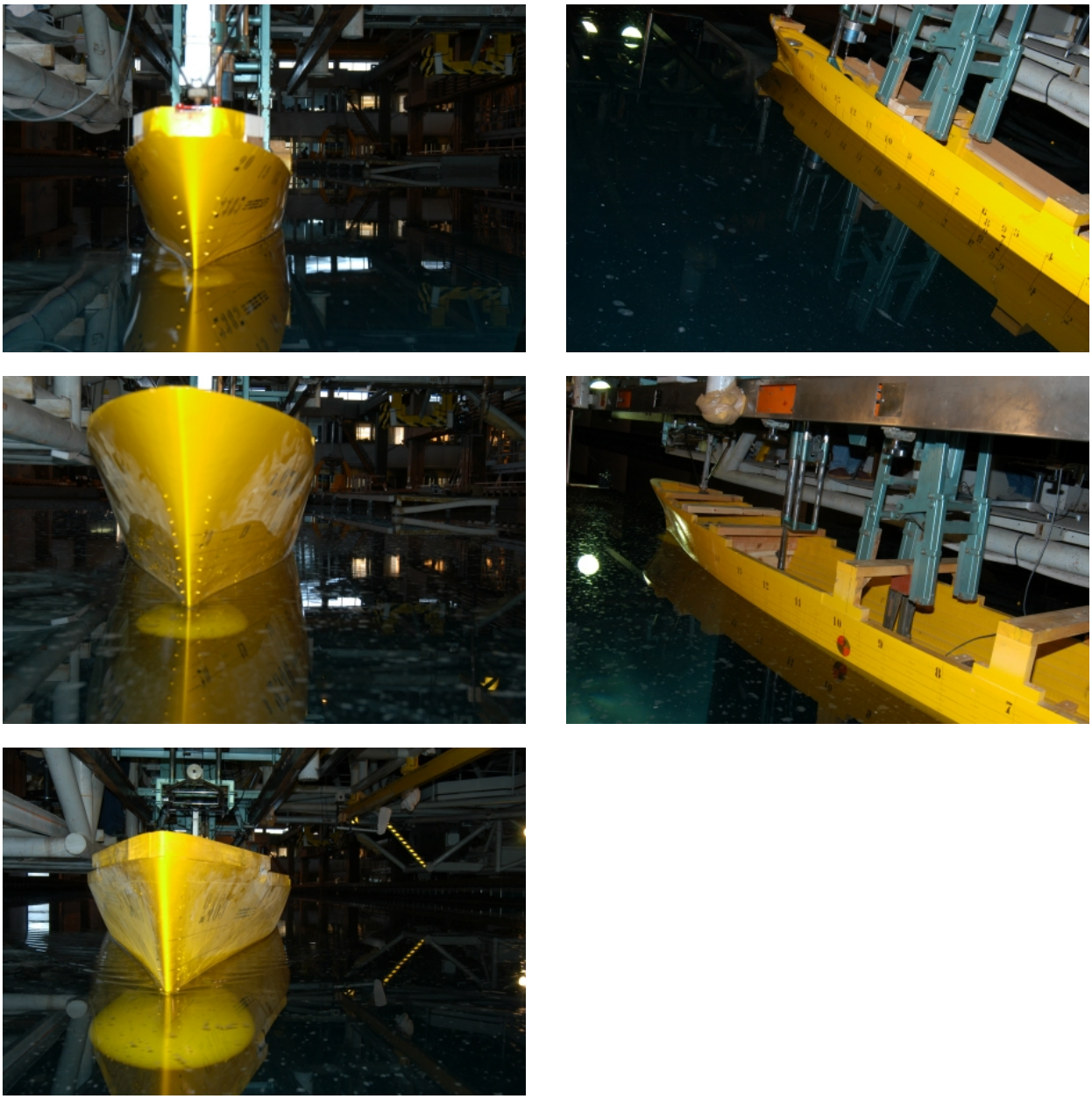

Figure 34: Photographs from the resistance tests, Froude 0.05. From top to bottom: models C.2385, C.2340 and C.2469.

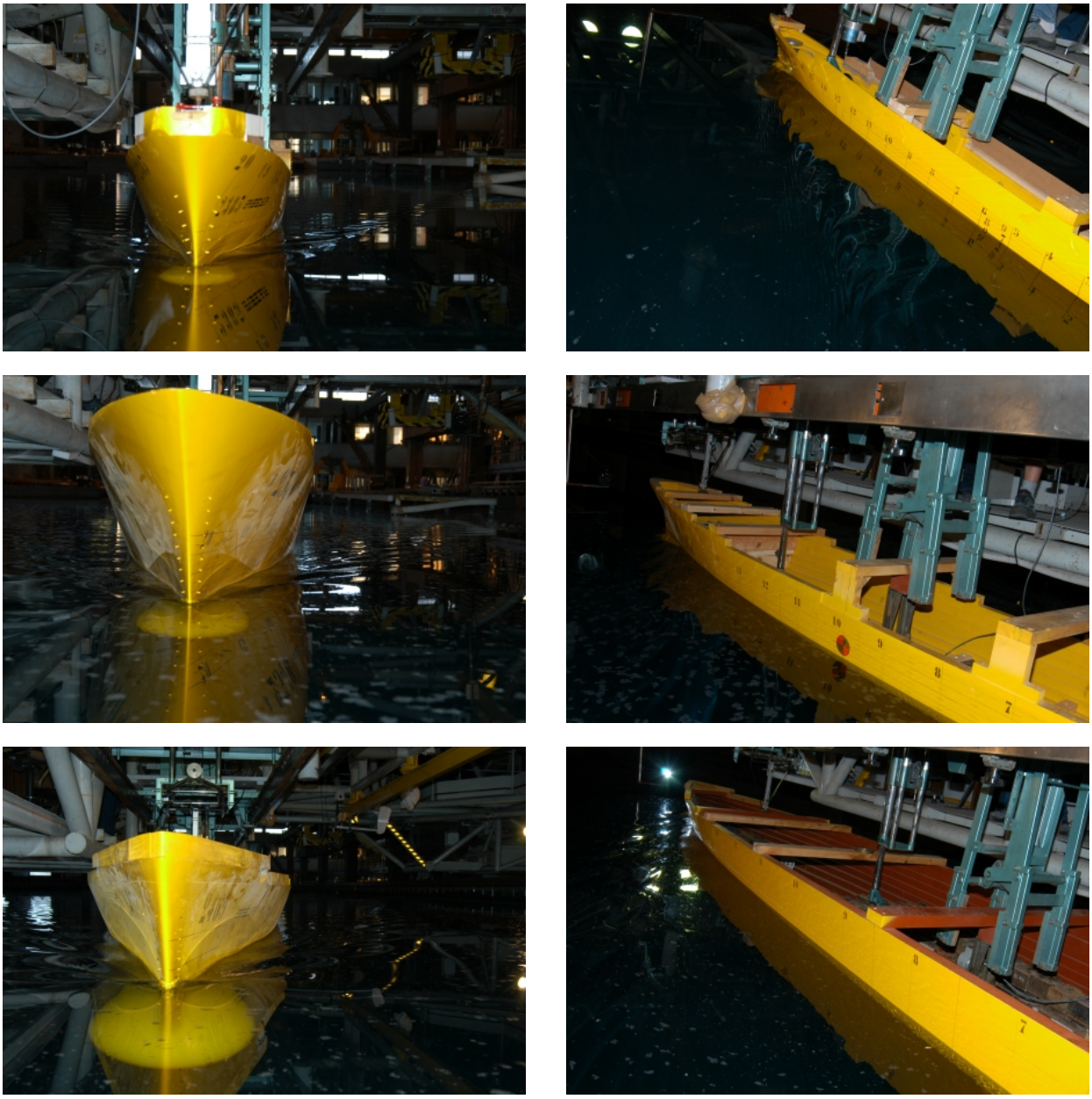

Figure 35: Froude 0.10. From top to bottom: models C.2385, C.2340 and C.2469.

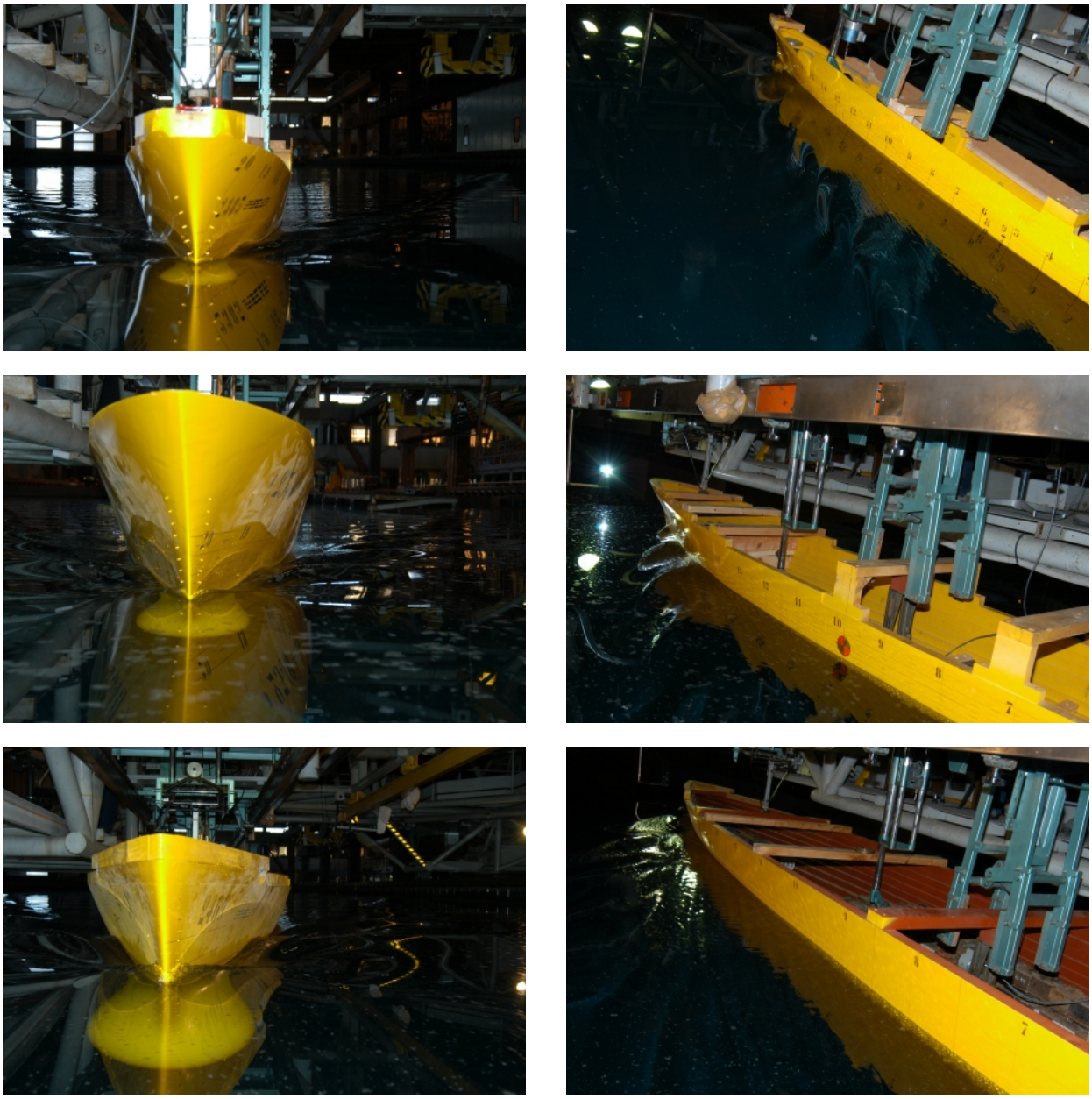

Figure 36: Froude 0.15. From top to bottom: models C.2385, C.2340 and C.2469.

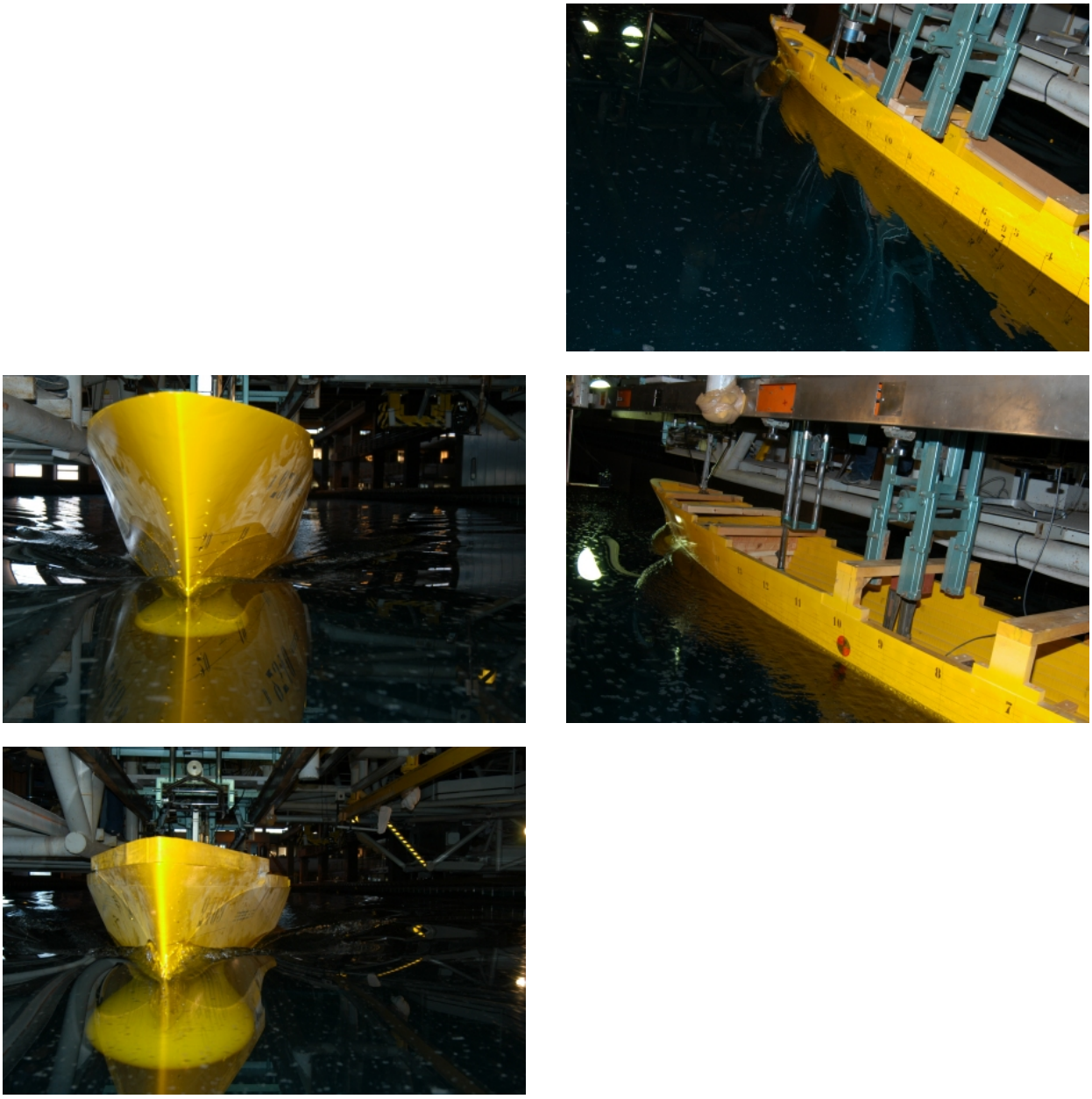

Figure 37: Froude 0.20. From top to bottom: models C.2385, C.2340 and C.2469.

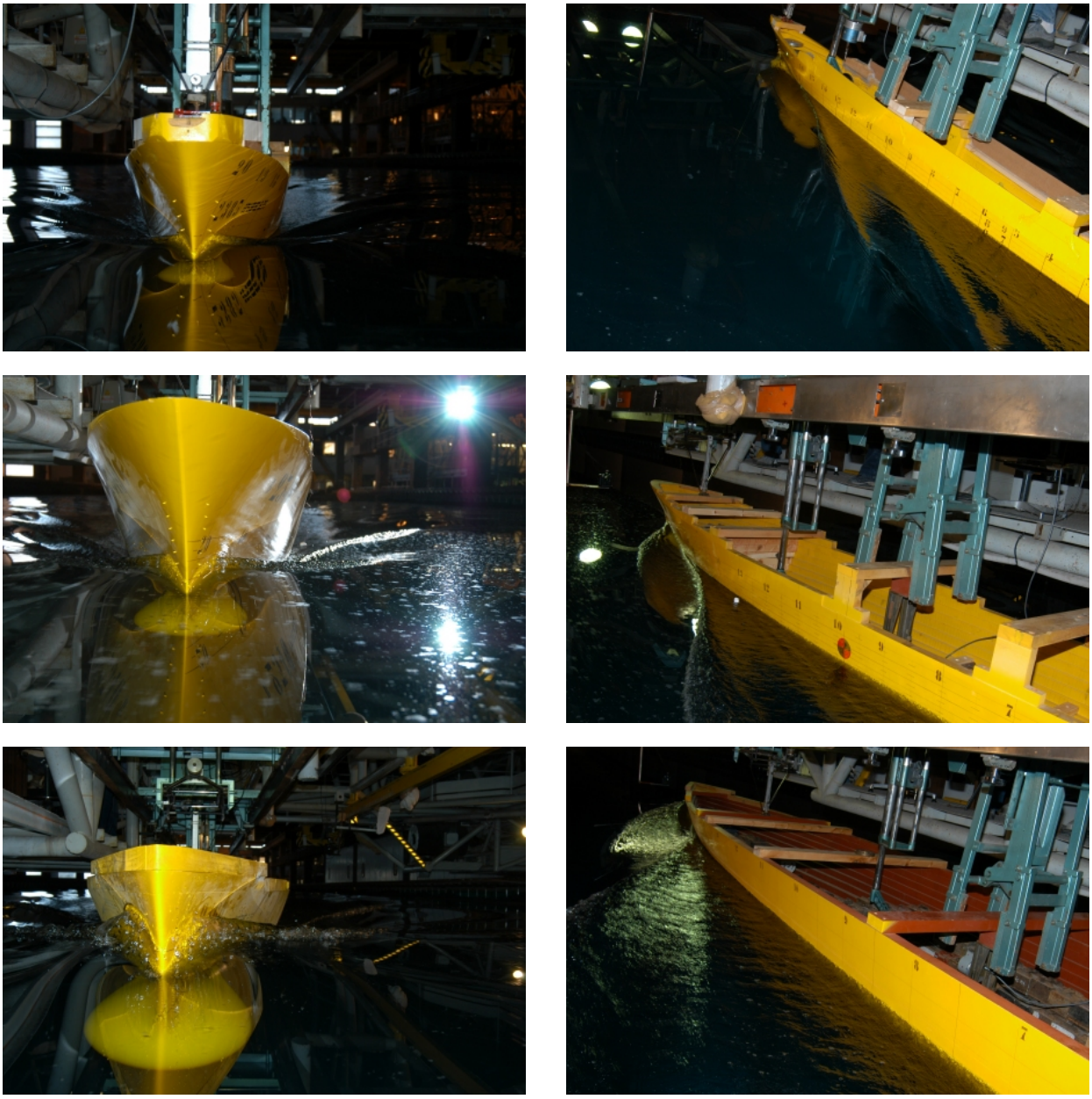

Figure 38: Froude 0.28. From top to bottom: models C.2385, C.2340 and C.2469.

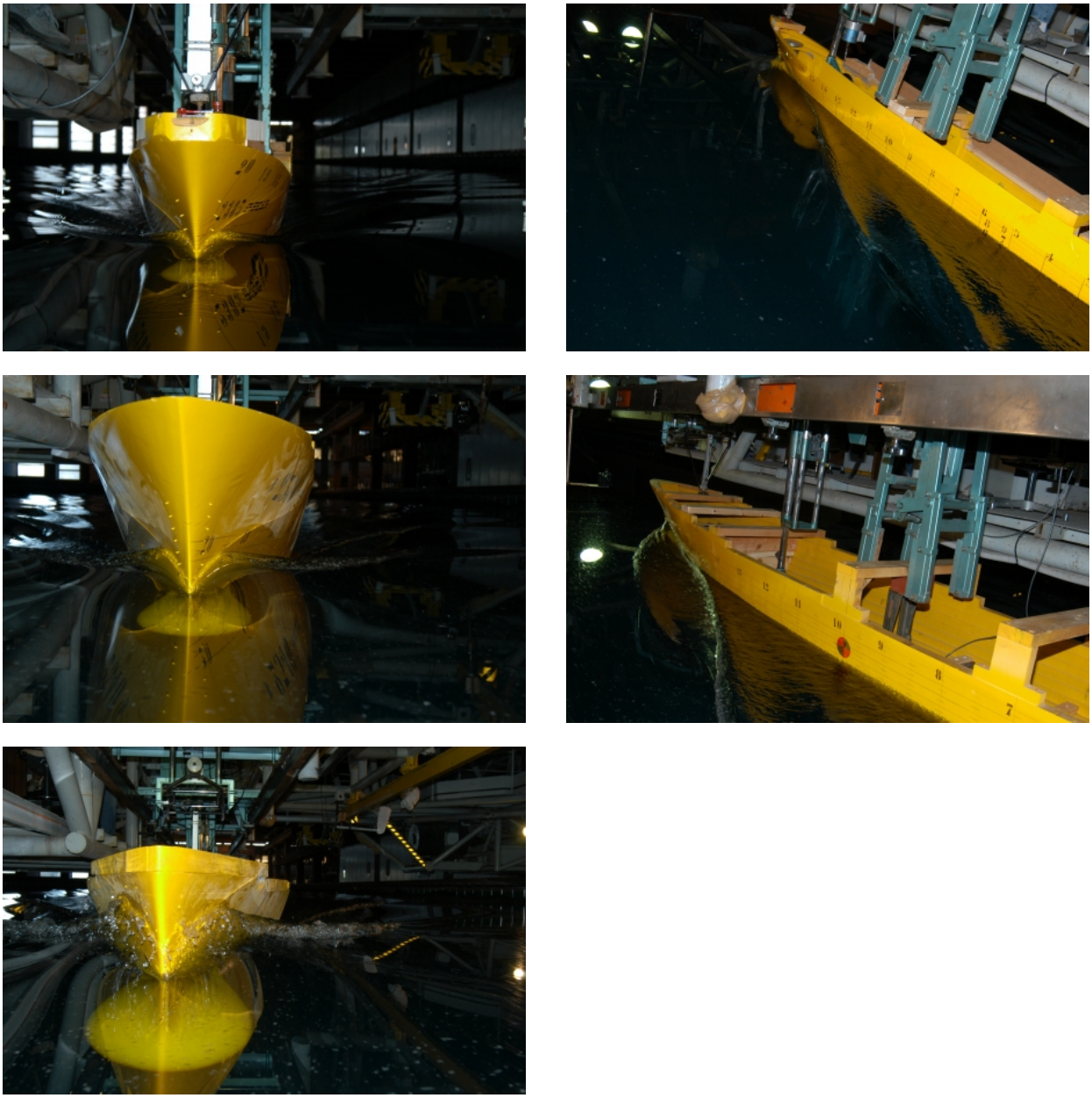

Figure 39: Froude 0.30. From top to bottom: models C.2385, C.2340 and C.2469.

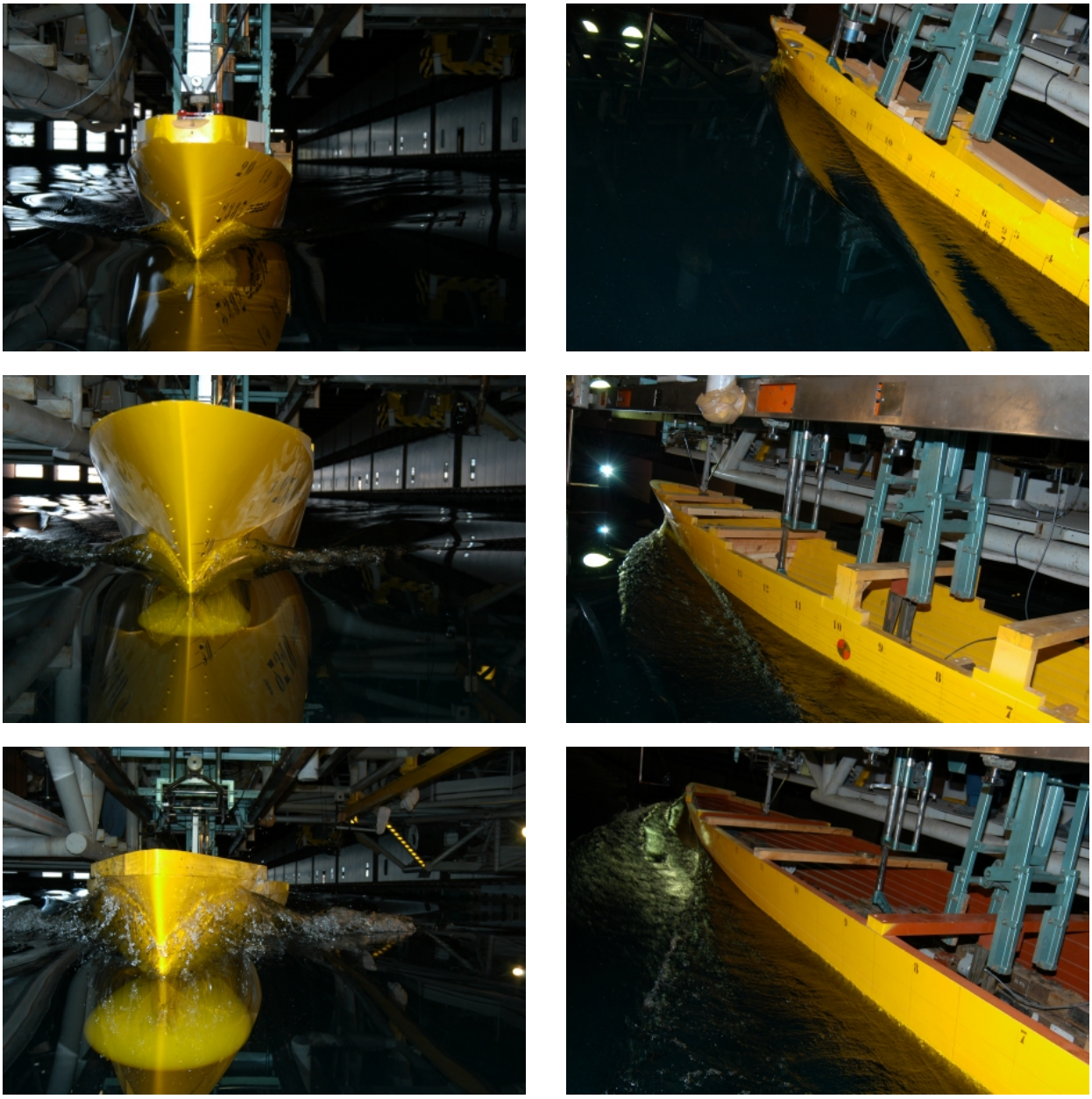

Figure 40: Froude 0.35. From top to bottom: models C.2385, C.2340 and C.2469.

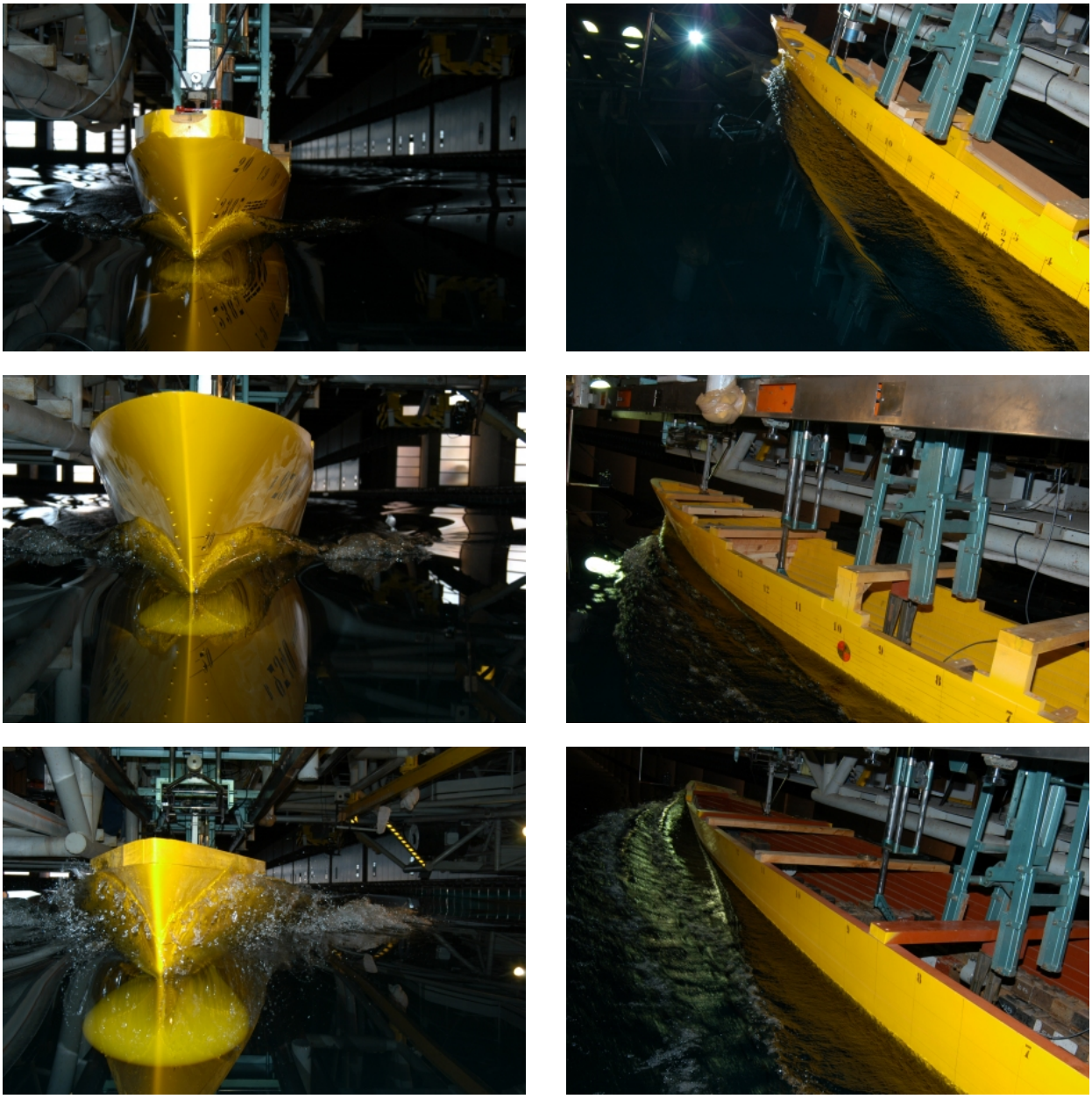

Figure 41: Froude 0.41. From top to bottom: models C.2385, C.2340 and C.2469.

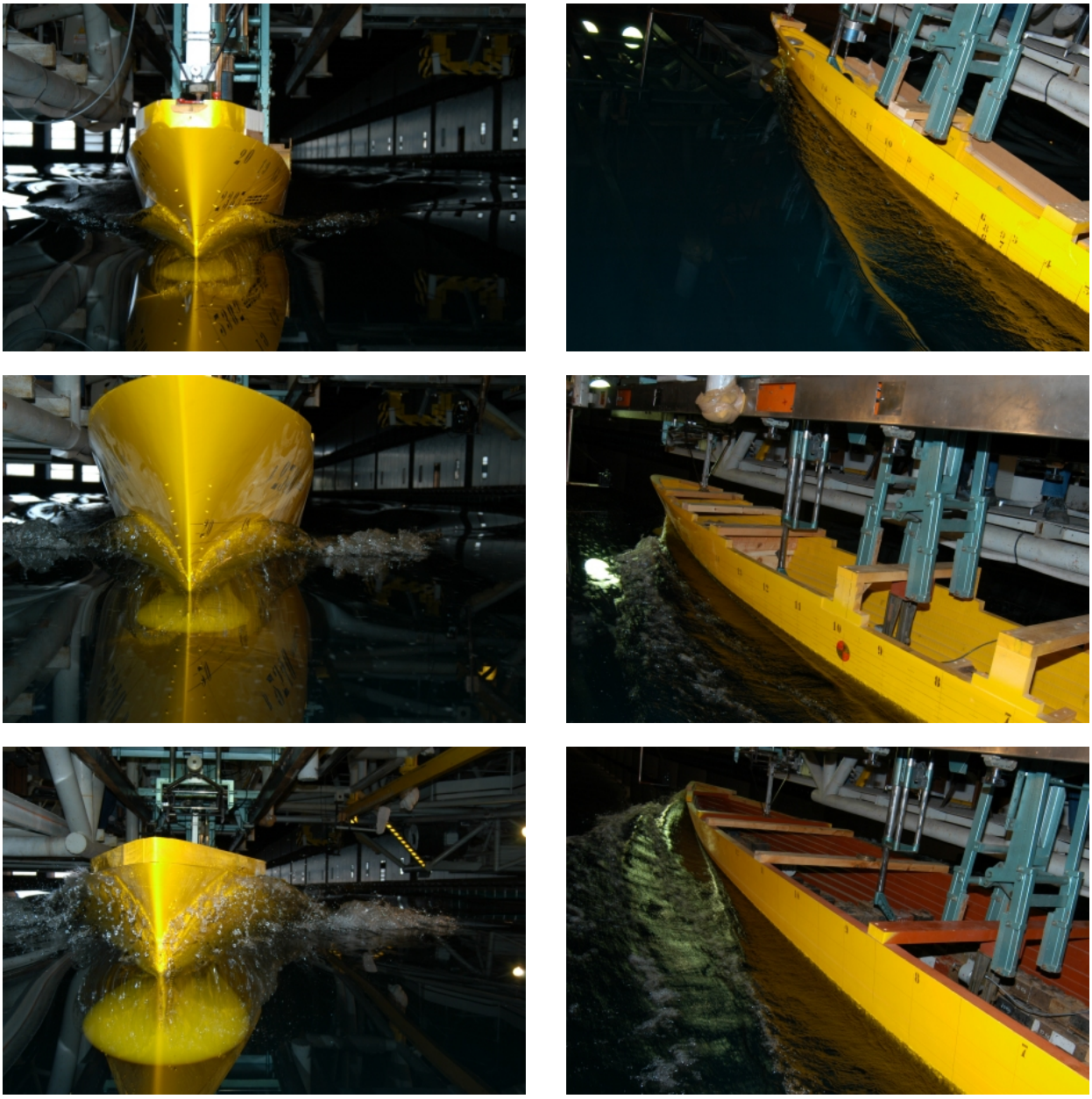

Figure 42: Froude 0.45. From top to bottom: models C.2385, C.2340 and C.2469.

5 Froude number 0.35

Pictures taken for the different scales and for different Froude numbers have been shown and discussed. These photographs provided a description of the near field water surface and of the bow wave breaking. While the measured resistance of the different models and successive analysis showed that there is a significant and quantifiable difference between the three scales. This chapter deals with the results of the measurements of the wave elevation pattern and mean flow velocity carried out with the larger model for one specific test condition. These measurements are conceived to give a quantitative indication of the evolution of the free surface and the flow field in conditions where the surface tension can be neglected. This is the case of model C.2469 towed at Froude number equal to 0.35. Due to its large dimensions the wavelength of the wave pattern around this hull is long enough to have an evolution towards the breaking that is not influenced by surface tension. Thus this case can be used for a better understanding of the wave breaking at full scale for real ships.

This condition was chosen on the basis of previous measurements relative to model C.2340 reported in [37]. Froude number equal to 0.35 was chosen because the bow wave breaking was quite steady and well developed. It will be shown in this chapter that increasing the model dimensions the wave breaking is not only more developed but also more stable.

In the first part of the chapter the measurements of the wave pattern and mean flow velocity of C.2469 ($\lambda = 14.32$) will be presented and discussed in detail. While in

the second part a comparison will be done with similar data obtained for the model scale of $\lambda = 24.824$, and reported in [37], and the differences will be highlighted and discussed.

5.1 Wave pattern measurements on the model C.2469

As it was described in the second chapter, dedicated to the experimental procedures, the wave elevation pattern was measured point by point following a regular grid of points drawn in the near field of the model. This measurement technique has the advantage that the wave elevation is acquired as a time history of what happens on the free surface point by point. Thus it is possible to calculate, not only the mean value of the wave elevation at a specific location, but also its *rms* value.

The data relative to each point were averaged over the acquisition time and, in a second step, the *rms* value was calculated. Both the values are normalized with the reference length L_{PP}; the equations are the following:

$$\overline{h} = \frac{1}{NL_{PP}} \sum_{t=1}^{N} h_t, \tag{25}$$

$$h_{rms} = \frac{1}{L_{PP}} \sqrt{\sum_{t=1}^{N} \frac{(h_t - \overline{h})^2}{N}}, \tag{26}$$

$T_S = n \cdot \Delta t$ is the total sampling time and N is the total number of samples taken at an interval $\Delta t = 1/1000\ s$.

Figure 43 is a 3D representation of the measured pattern, the grid lines are left so to make the measurement points visible. The water surface is colored with the average value of the wave elevation. In the next figure 44 the average wave eight together with its *rms* are presented in plan view. As expected the crest of the bow wave is over the undisturbed water level, whereas the crest of the shoulder wave is under the zero level and recovers elevation only going far from the hull. The *rms* of the wave elevation gives an indication of *how much* the signal, namely the wave elevation, oscillates in that point.

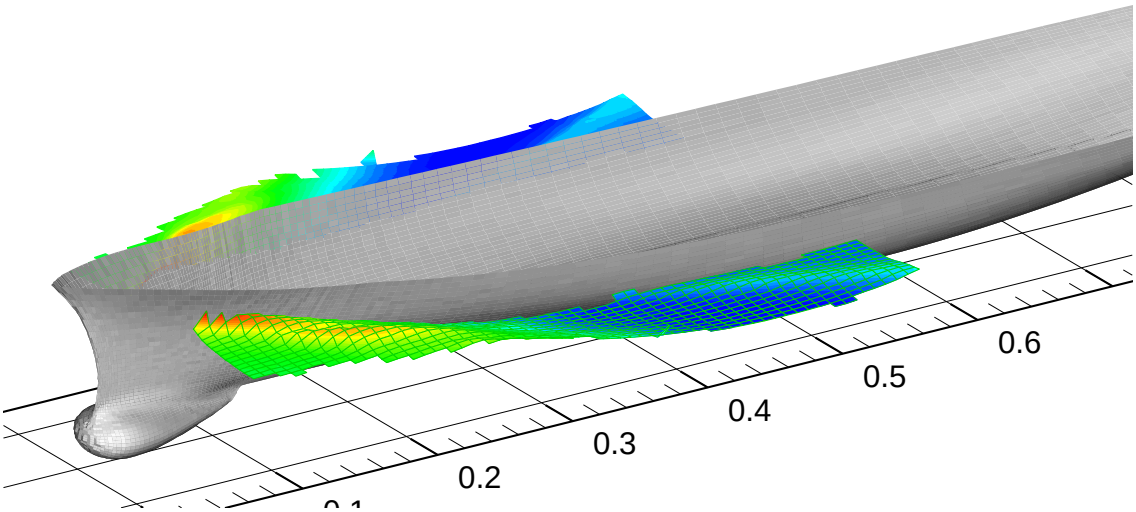

Figure 43: wave elevation pattern plotted from the measured data in the near field of C.2469.

Looking at the bow wave in the mean wave elevation plot (top of figure 44) two zones of maximum wave elevation (in red) are clearly visible. This is due to the fact that at these conditions the bow wave of model C.2469 overturns and its crest impacts on the undisturbed water generating a splash up (figure 45) and the subsequent secondary crest.

In absolute values, the maximum mean wave elevation is 210 mm reached on the bow wave crest, whereas the minimum value (-101 mm) is located on the rear trough just below the shoulder wave.

The entire crest of the shoulder wave lays under the mean water level, the minimum height of -58 mm is reached close to the hull, then, following the crest line, away from the hull, its height increases reaching the value of $\simeq -24$ mm at the bound of the measured field.

Figure 46 is a comparison between the measured data and a photograph at the same condition. The plot on the right is rotated so to offer a similar point of view. The averaged wave height is colored with the rms values of the wave elevation. Interestingly the maximum rms values are located at the breaking crest of the

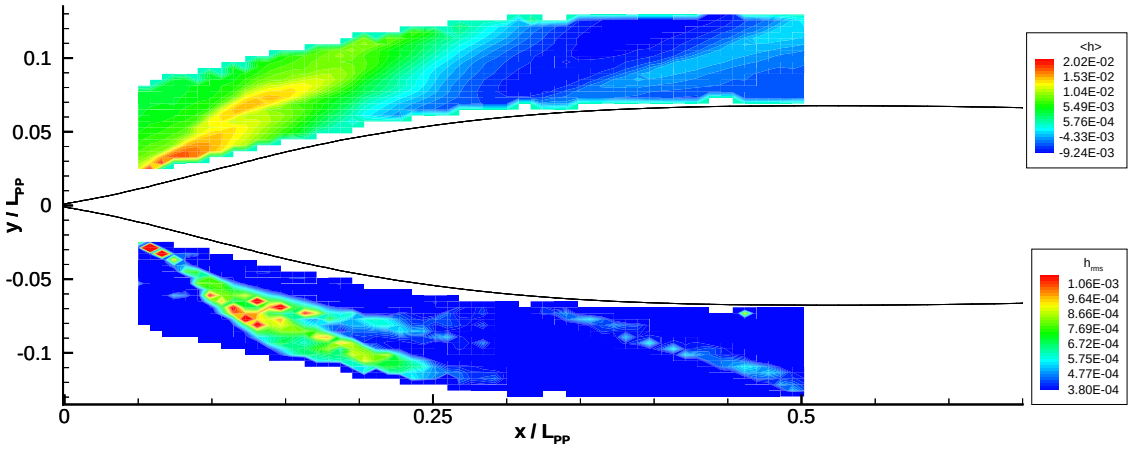

Figure 44: measured wave pattern relative to C.2469. Averaged wave elevation $\overline{h}$ (top) and h_{rms} (bottom).

bow wave (A), on the breaking crest of the shoulder wave (C) and on the free surface scar generated by the second splash up of the crest of the bow wave (B). The presence of white water enhances the visibility of the scar. This comparison between the photograph and the measured data shows that the area of high rms value and the location of the scar correspond. This is an index of surface turbulence in correspondence to the splash up scar.

The areas of high rms are very well defined in the plot of figure 44. As can be seen also from the photographs relative to this scale (figure 40) the near field wave pattern is very stable and its boundaries are very well defined. In fact the plunging type breaker impacts on the undisturbed surface upstream. The capillary wave train on the front face of the breaking wave is completely cancelled by the splash up and the water surface changes abruptly from smooth conditions to breaking.

5.2 Mean flow measurements on the model C.2469

The mean flow velocity was measured in three different transversal sections of the model C.2469 towed at $Fr = 0.35$. The main parameters of the experiment are

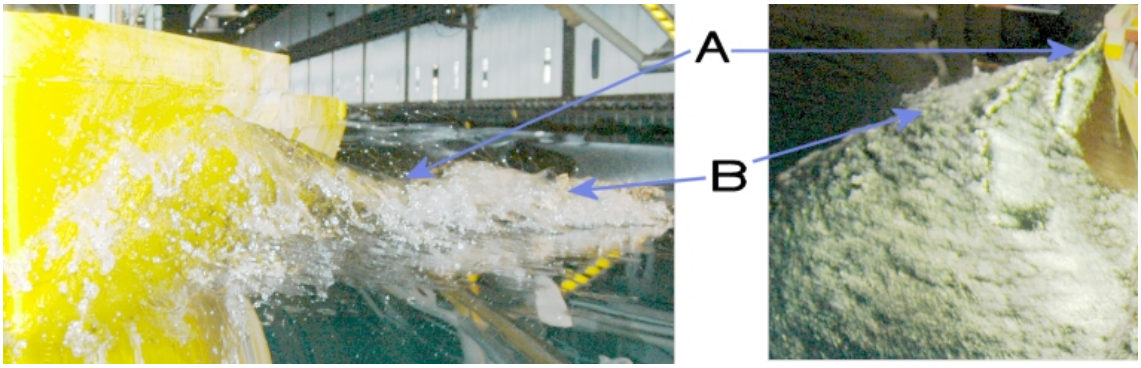

Figure 45: the bow wave and its splash up on the bow of C.2469 at $Fr = 0.35$.

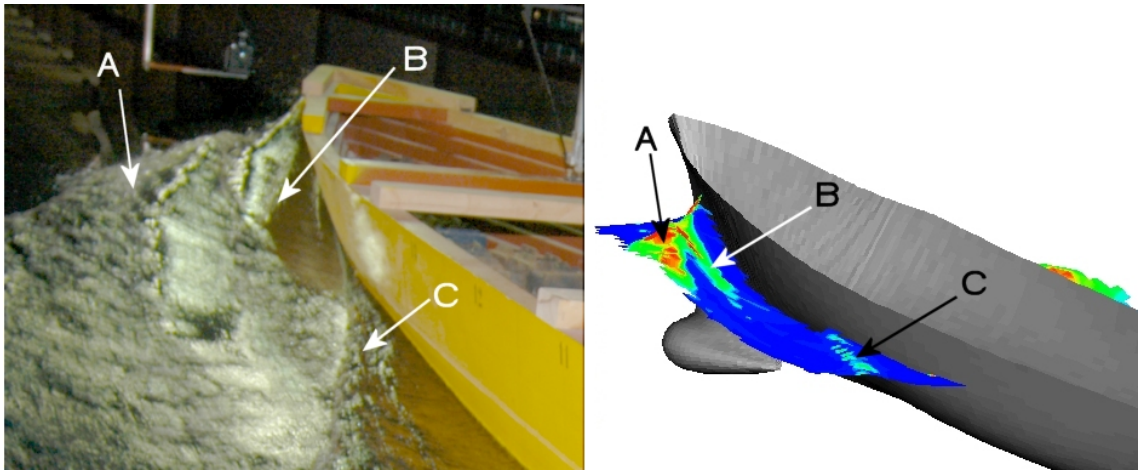

Figure 46: wave elevation pattern measured in the near field of C.2469. The colored contour represents the rms value of h.

summarized in table 5.

The sections will be named with a number that is the distance of the section from the bow divided by the total length so $SectionName = x_{section}/L_{PP}$. The section more close to the bow is section 0.20, followed by 0.35 and 0.40. Their relative position can be viewed together with the measured wave pattern in figure 47 for better understanding. The colored areas superimposed on the wave pattern are the values of h_{rms}, that is an indication of where the breaking occurs. Section 0.20 is in the bow breaking area, the mean water level is above the undisturbed free surface.

	C.2469 flow velocity measur.
facility	basin n°1
location of measurement planes (sections)	(020L_{PP}) (035L_{PP}) (040L_{PP})
n° of points	3709
sampling freq. [Hz]	100
acquisition time [seconds]	5
test speed [m/s]	3.451 [Fr=0.35]

Table 5: main parameters of the velocity flow measurement tests for C.2469 at $Fr = 0.35$.

The flow on section 0.35 was measured to gather information about the location where the shoulder wave originates and the acquisitions on section 0.40 can give indications about its evolution. These two sections are located in the wake of the breaking bow wave.

Figures from 49 to 51 show the plots of the measured velocity and of the calculated longitudinal vorticity on the three different sections. Velocity is plotted in the top frame of every figure and longitudinal vorticity on the bottom one.

The absolute value of the velocity is normalized with the undisturbed velocity test $v_{Fr=0.35} = 3.451\ m/s$, the linear dimensions with L_{PP}. The vectors represent the velocity components on the yz plane. The reference vector is showed in figure 50 (top). The colors are the levels of the longitudinal component of the measured velocity v_x and its values are shown on the legend above each plot. The outer contour of the correspondent section of the hull is partially showed. The mean measured wave elevation line is plotted with continuous line together with two dashed lines that represent $(\overline{h} + h_{rms})$ and $(\overline{h} - h_{rms})$.

On the bottom frame of figures 49-51 the longitudinal component of the vorticity is plotted as colored contours under the mean water level. The longitudinal component of the vorticity vector was calculated from the velocities on the yz plane in the

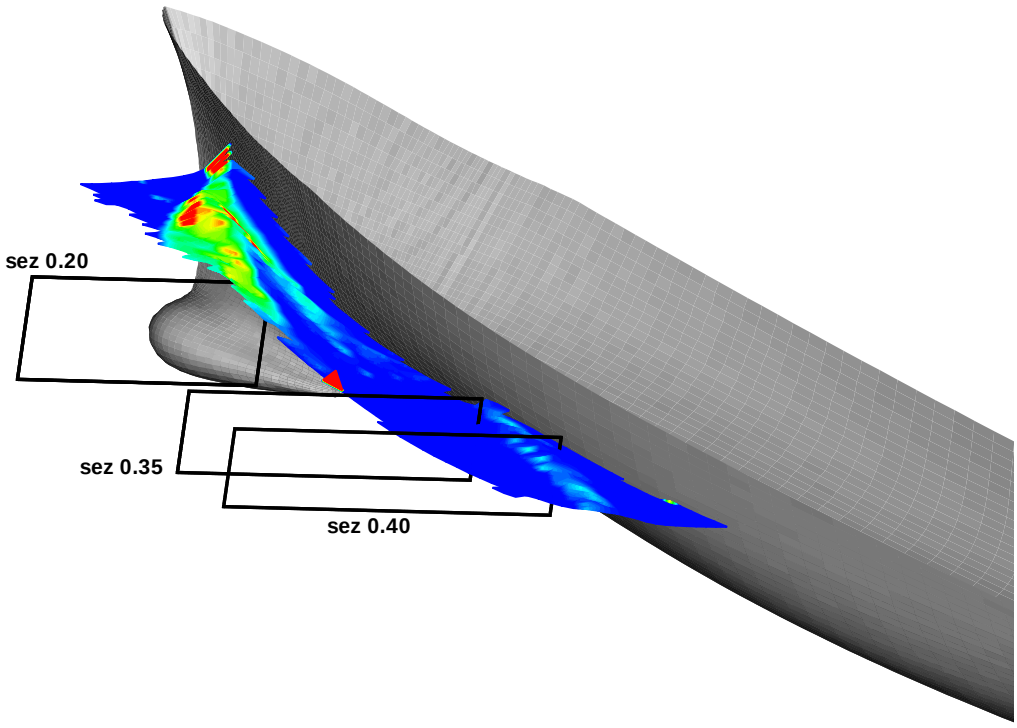

Figure 47: position of the three transversal sections where the mean flow was measured on model C.2469.

following way:

$$\omega_x = \frac{\partial v_z}{\partial y} - \frac{\partial v_y}{\partial z}, \tag{27}$$

being v_y and v_z the velocity components on the section plane. The partial derivatives were calculated with centered differences numerical algorithm.

Figure 49 show the section in correspondence of the breaking bow wave and, on the wave elevation plot, the scar is visible at $y = -0.11$. This is also the location with maximum rms of the wave elevation. On the sides of the scar, there are two points of maximum wave elevation. Under these crests there is the maximum velocity defect. Here the modulus of the normalized velocity $|v|$ is equal to 0.83.

In the velocity plot of figure 50 it is possible to recognize the origin of the shoulder wave from the mean wave elevation plot. The maximum of the shoulder crest is

negative $-8.27 \cdot 10^{-2}$ at $y = -0.057$. The entire measured section and the free surface lays entirely under the level of the undisturbed free surface. The minimum of the surface elevation corresponds to the wake of the breaking bow wave. Under this minimum the flow velocity overtakes the value of 1: the flow is accelerated till $|v| = 1.049$. Farer from the hull the free surface is still plane and undisturbed.

Figure 51 is relative to section 0.40, very close to the preceding section 0.35. The same mean surface profile is recognizable translated externally, the maximum and the minimum have moved outwards from the hull together with the shoulder wave crest. The velocity defect has followed the crest of the shoulder wave and the velocity excess is still under the minimum elevation of the surface. The location where $v_y = 0$ did not move. The maximum of the velocity modulus is $|v| = 1.09$.

The plots of the longitudinal vorticity of figures 49, 50 and 51 display areas of positive and negative vorticity. At section 0.20 the area of positive vorticity closer to the hull is located between $y = 0.09$ and $y = 0.097$, the second between $y = 0.11$ and $y = 0.13$. On the following sections two areas of positive vorticity are also visible. On section 0.35 the outer area positive vorticity is bounded between $y = 0.088$ and $y = 0.093$ and the inner can be seen for $0.11 < y < 0.13$. At section 0.40 the bounds of the two areas are $0.085 < y < 0.097$ and $0.11 < y < 0.13$.

The vorticity does not substantially change transversal position, with respect to the center line of the hull, from section to section. This fact reveals the presence of a stable vortical structure, with axis parallel to the longitudinal direction, that exists along the measured area and probably also downstream. This observation is consistent with the hypothesis that the vorticity is originated at the impact of the crest of the breaking bow wave, with the underlying free surface, and it is convected downstream by the mean flow in vortex tubes.

Close to the areas of maximum positive vorticity the blue areas of negative vorticity are visible. Also the location of the negative vorticity, visible close to $y \simeq 0.1$, does not change from section to section. Due to the dimensions of the Pitot's head it was

not possible to investigate in the small area between the measured points and the trace of the free surface, where no vectors are drawn in the plots. The reason is that, very close to the free surface, the head of the Pitot is always at risk of going out of the water and the velocity measurements could not be validated in this area. Thus we can only guess from the plot relative to section 0.40 (figure 51) the presence of negative vorticity in this location.

The velocity vectors relative to the on plane components of the velocity field v_y and v_z are directed towards the location of maximum v_x that is under the wave crest. The maximum of the vorticity was calculated in the same region. These trends are consistent with the hypothesis that the vorticity is organized in rolls with longitudinal axis that remain under the surface.

5.3 Comparison between two scales

Wave elevation pattern and mean flow was measured on the model C.2340 towed at the same conditions as the larger C.2469 till now described, Froude equal to 0.35 and fixed sinkage and trim conditions. Details and results, also about flow maps relative to additional transversal sections, can be found in [37].

In figure 52 the wave elevation patterns measured on the two models are shown together for comparison. The lengths and the velocities have been normalized with the correspondent reference values. The maximum of the wave elevation is 0.21 for for C.2469 and 0.18 for C.2340, the minimum value -0.01 for both cases.

The major difference between the maps is relative to the bow wave. Two crests are clearly visible on the plot relative to the large model of figure 52, this double peak is a consequence of the splash up. On the plot relative to C.2340 the crest of the bow wave is only one. The reason is that the surface tension inhibits the formation of the overturning motion of the breaking crest (see also [17] and [43]) and suppresses the splash up thus changing the evolution of the plunging breaker. The two photographs of figure 48 are relative to this test condition for the two model

scales here considered and clearly show this situation in reality. The wave pattern

Figure 48: same portion of wave field photographed for the two larger model scales at $Fr = 0.35$. Middle scale C.2340 is on the right and large scale C.2469 on the left.

relative to model C.2469 (figure 52) is more defined, its bounds are more net. The region interested by intense surface turbulence due to the breaking is more extended in the smaller model case. The large model displays a breaking crest where intense surface turbulence is more confined in the forward part of the crest as the more intense breaking seem to be able to damp more the disturbances in the wake. This observation is consistent with the plots of the rms of figure 53, comparison of the two scales. The area of high rms is much more extended on the pattern relative to the smaller model. Also the shoulder wave crest is more unstable in the C.2340 case, together with the whole area between the bow and the shoulder wave. On the same way the scars are much more visible in the larger scale model than on C.2340. In the figures 54 and 56 the mean flow velocity maps for section 0.20 and section 0.40 are shown for comparison between C.2340 and C.2469, together with the mean wave elevation on the section and its rms value, the top plots are relative to C.2469 and the bottom ones to C.2340. Both maps have been normalized with the correspondent reference lengths and test velocities.

For section 0.20 (figure 54) it is possible to see that the measured area relative to C.2340 is smaller (the bounds of the measured areas relative to C.2340 have

been reported on the plots relative to C.2469 for better comparison between the measurements), the only minimum of the velocity that can be seen on the plot of C.2340 is basically on the same position for both model scales. The other minimum of the velocity is under the second crest ($y \simeq -0.12$) and cannot be measured on the smaller scale simply because, the waves are smaller, but the Pitot is always of the same physical dimensions, thus the resolution in this case is halved.

Similar considerations can be done for the vorticity plots of figure 55, that are derived from the same velocity data. The big area of positive vorticity with center at $y \simeq -0.094$ is in the same position for model C.2340.

The flow maps for section 0.40 are plotted in figures 56 and 57. Again the trends are basically the same and it is confirmed that the free surface is more stable for the bigger scale. The minimum velocity that is barely visible on the plot of the velocity of C.2369 (figure 56 top frame) is more visible on C.2340 exactly in the same position. The vorticity plots of section 0.40 have a common positive area under the crest of the shoulder wave.

In the plots of figures 55 and 57 same color range have been used to highlight the vorticity. It can be pointed out, looking at 57, that the vorticity in the field of C.2469, large model, is more intense as the red color, indicating the positive vorticity, is more intense. But also a different approach can be used to compare the vorticity on the two different scales. Since the maximum value of the vorticity can depend on the resolution of the instrument this value in not significative for the purpose of evaluating the strength of the vortex it is then possible to consider only the areas where the vorticity is greater than a certain common threshold value. When the area occupied by the offset level is greater it means that the vortex is stronger independently of the value of the maximum inside.

The plot relative to section 0.40 (figure 58 right column) is more useful than 0.20 on this point of view because the vortical area is all bounded. The greater extension of the area occupied by the positive vorticity above the value of $\omega_x = 2$ (green) and

$\omega_x = 4$ (red) for the flow of C.2469 confirms that the vortex is stronger for the larger scales.

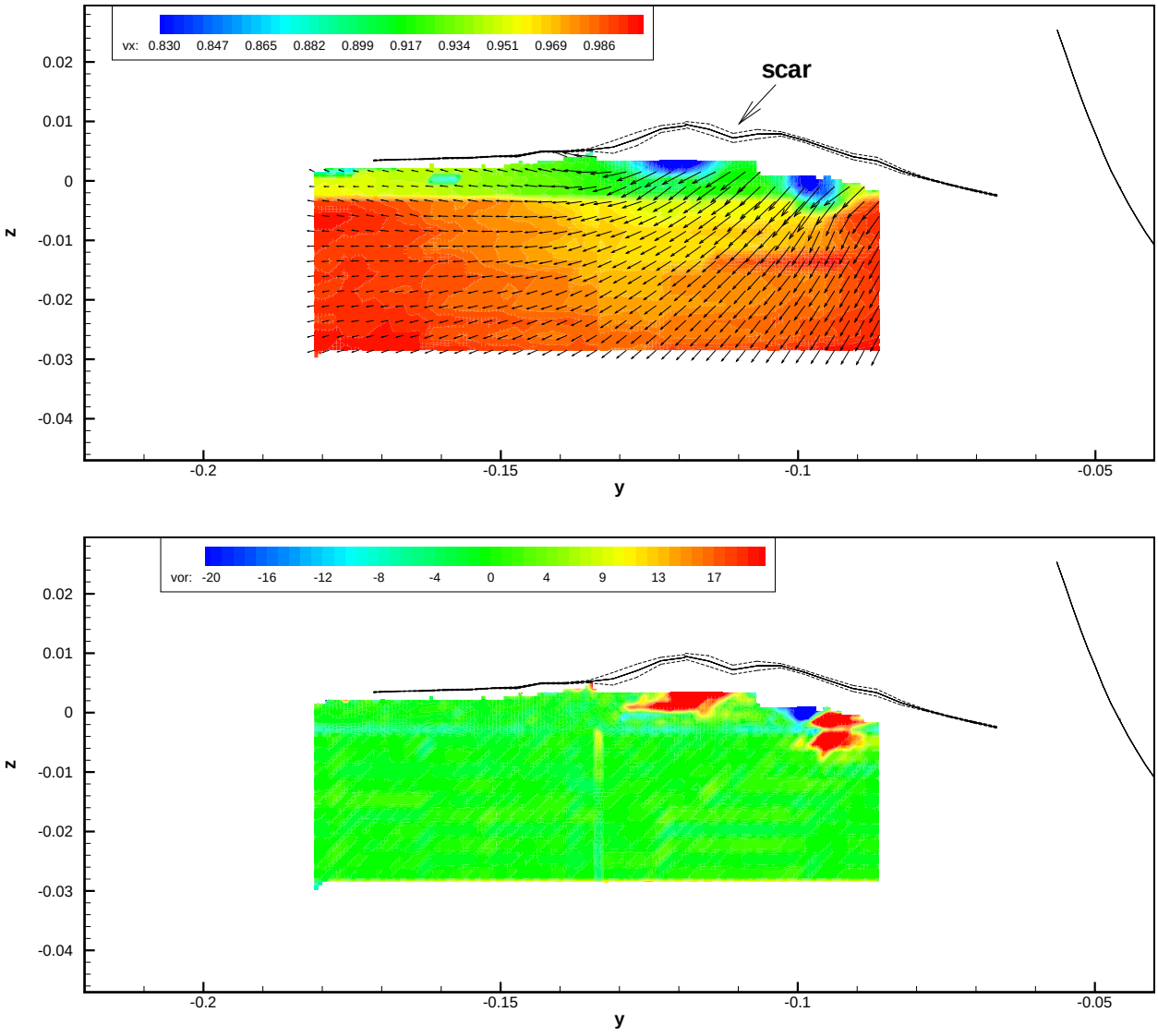

Figure 49: velocity (top) and vorticity (bottom) flow maps measured at section 0.20 for model C.2469 at $Fr = 0.35$.

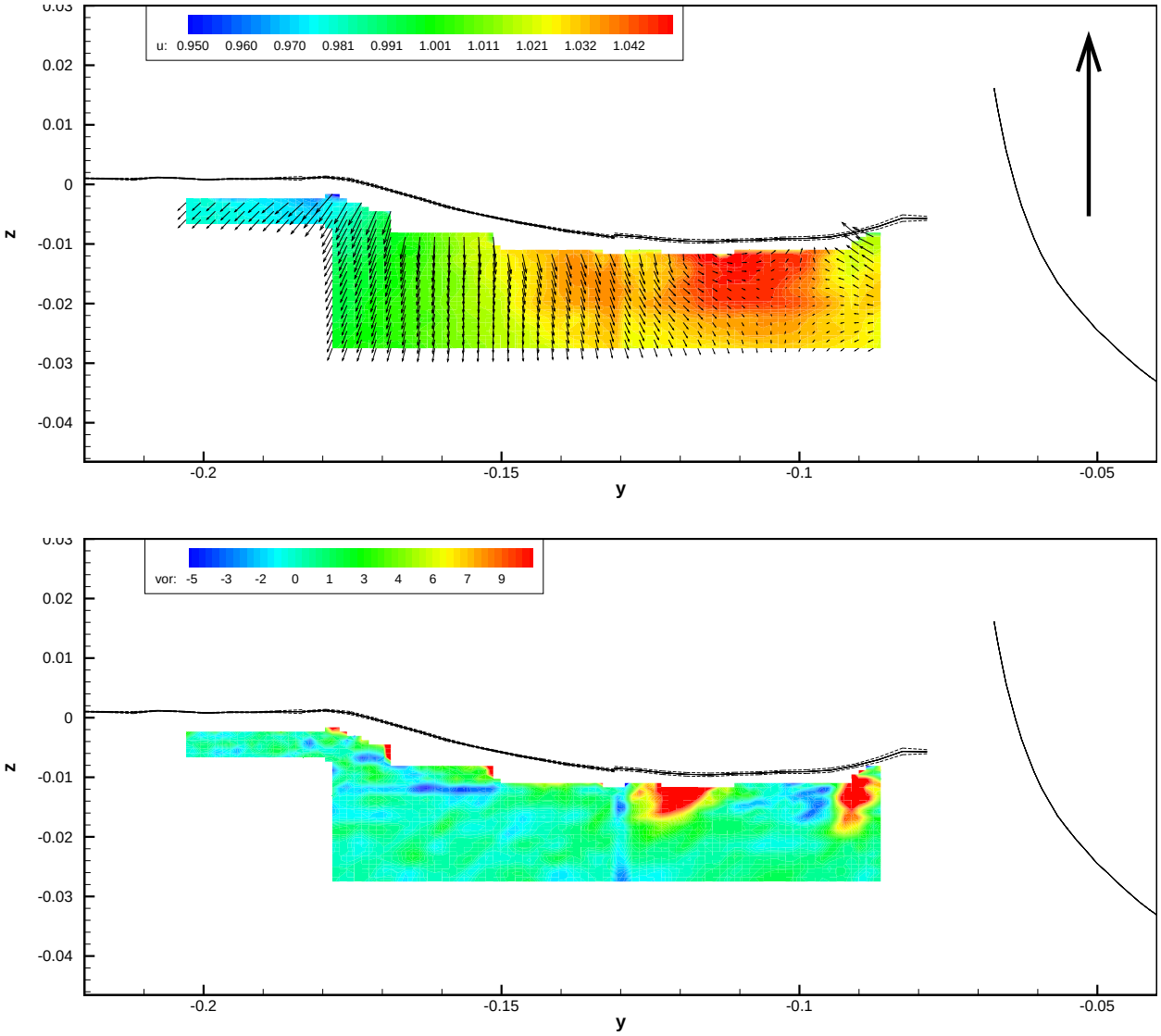

Figure 50: velocity (top) and vorticity (bottom) flow maps measured at section 0.35 for model C.2469 at $Fr = 0.35$.

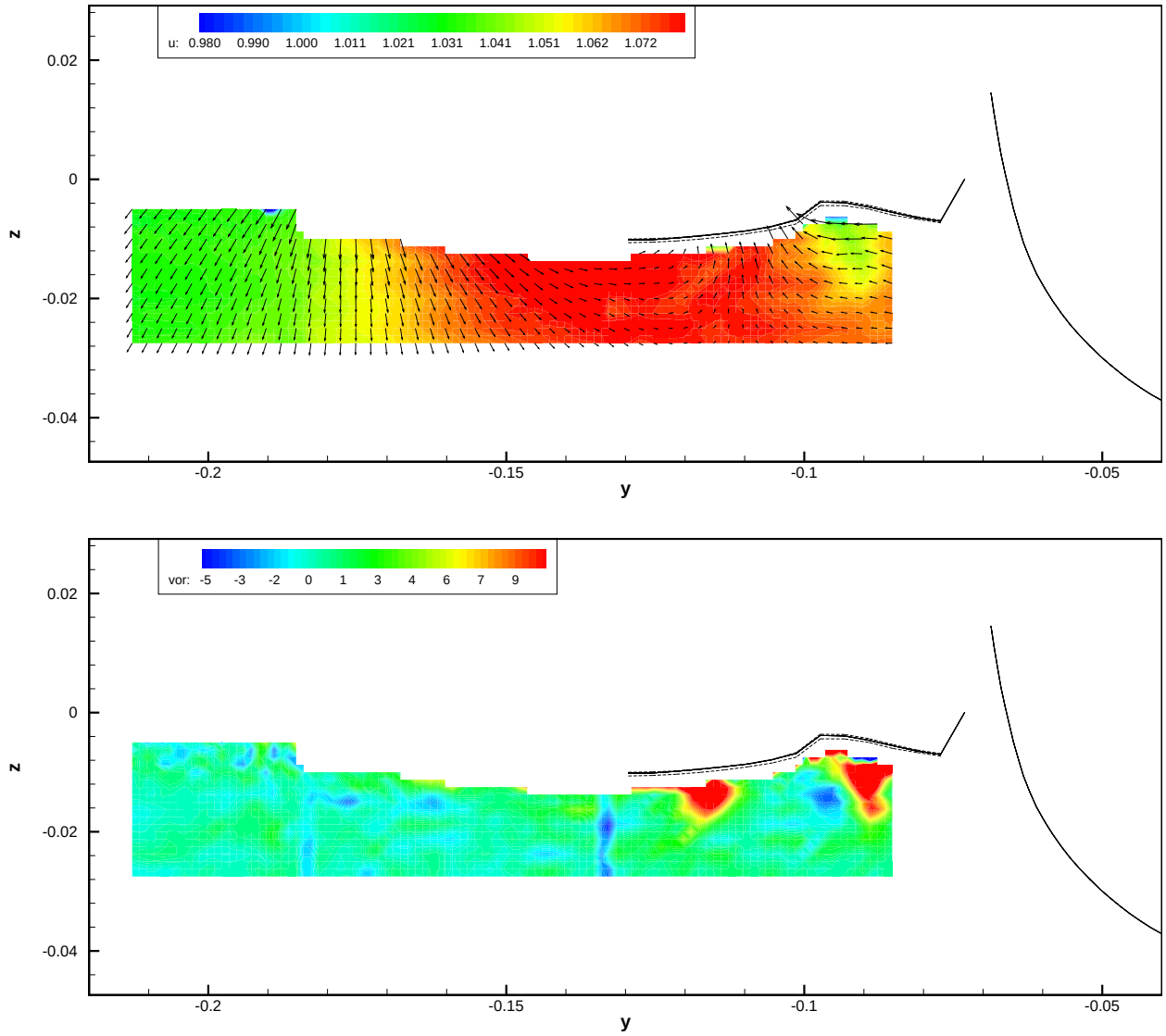

Figure 51: velocity (top) and vorticity (bottom) flow maps measured at section 0.40 for model C.2469 at $Fr = 0.35$.

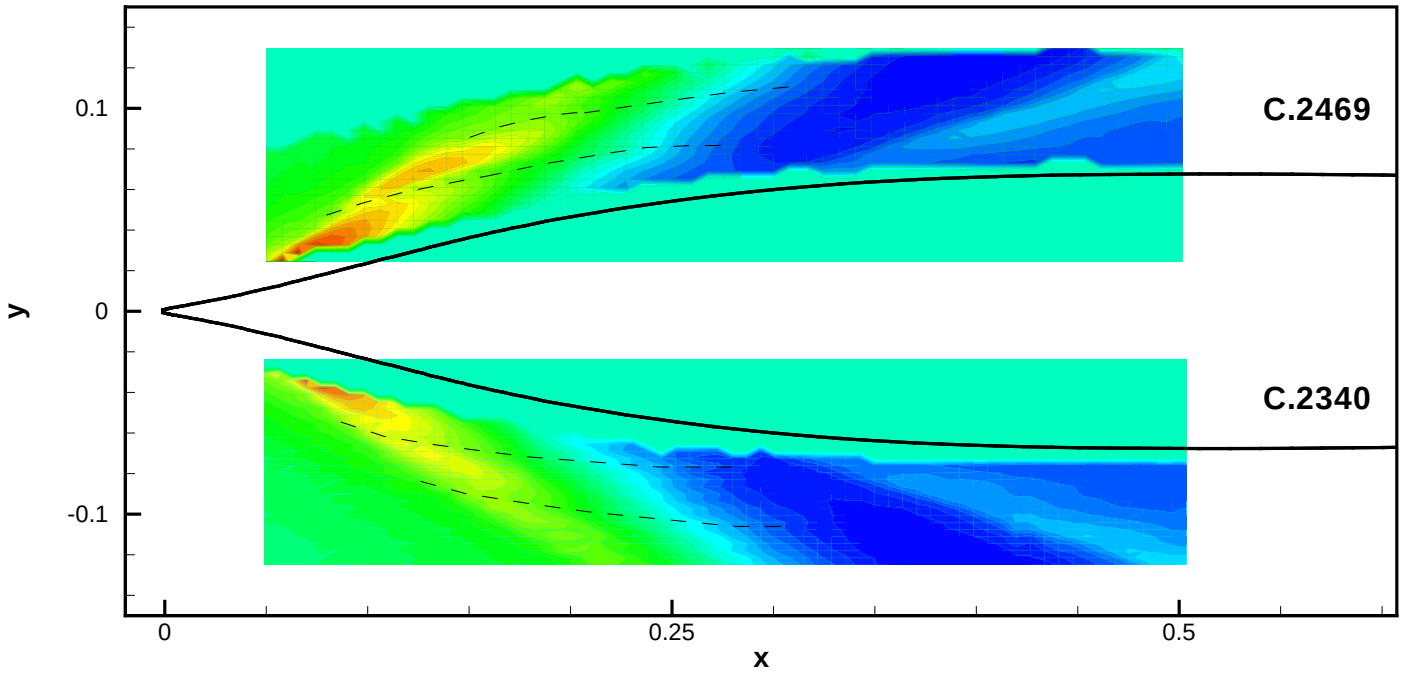

Figure 52: comparison of the mean wave elevation $\overline{h}$ for the case of the large scale model (top) and the middle scale one (bottom). The dotted lines show the location of the surface scars as locus of the minimum of the mean wave elevation. The data relative to C.2340 is taken from [37].

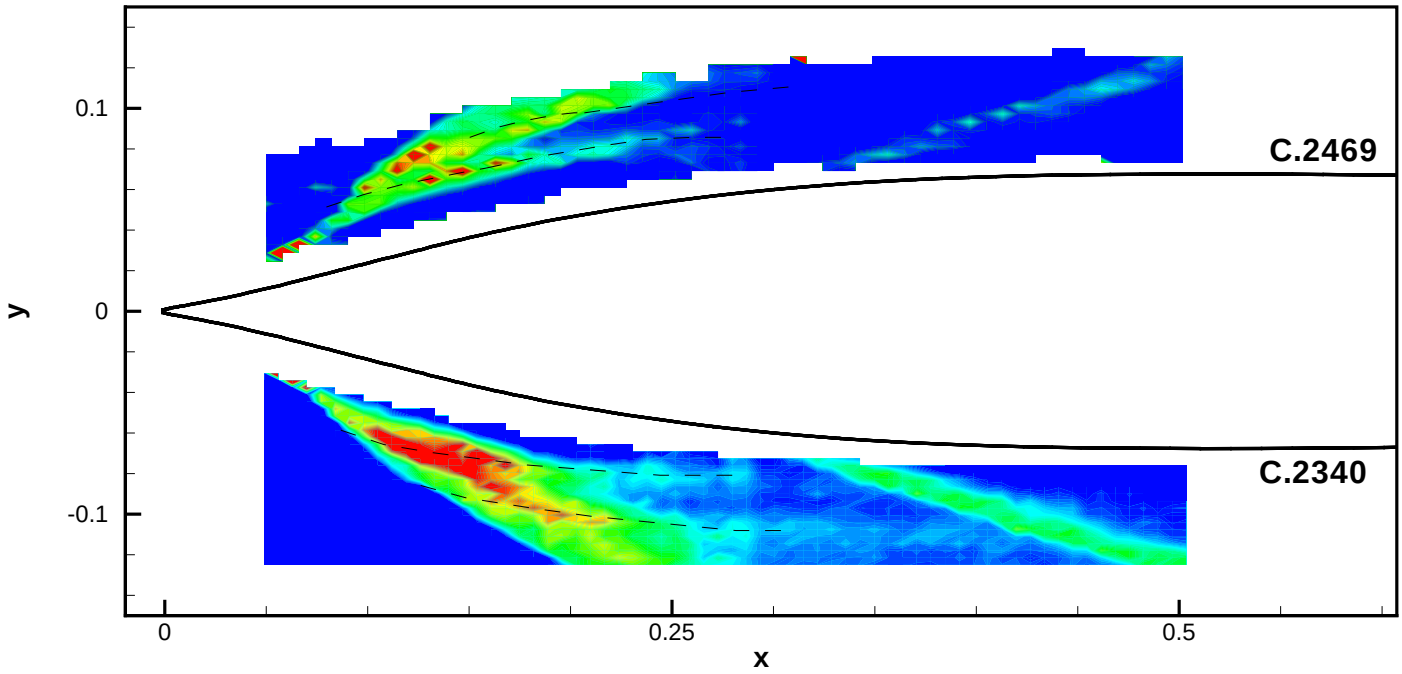

Figure 53: comparison of the root mean square value of the wave elevation h_{rms}. Large scale model on top and the middle scale on bottom. The dotted lines show the location of the surface scars as locus of the high rms of the wave elevation. The data relative to C.2340 is taken from [37].

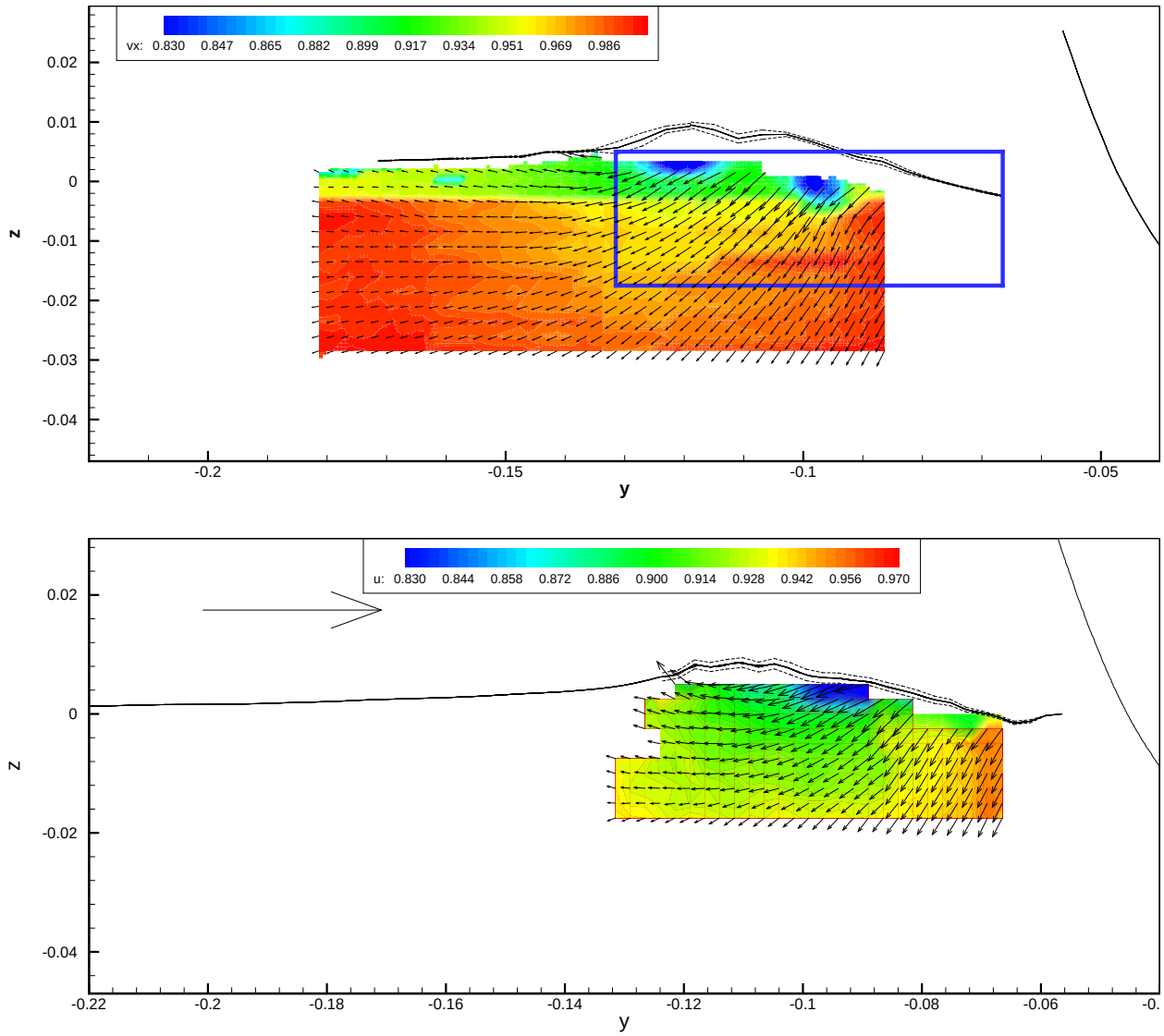

Figure 54: comparison of the flow maps relative to section 0.20 for the large model scale C.2469 (top) and the middle model scale C.2340 (bottom). The blue contour represents the bounds of the measured area of C.2340 reported on the plot relative to C.2469. The data relative to C.2340 is taken from [37].

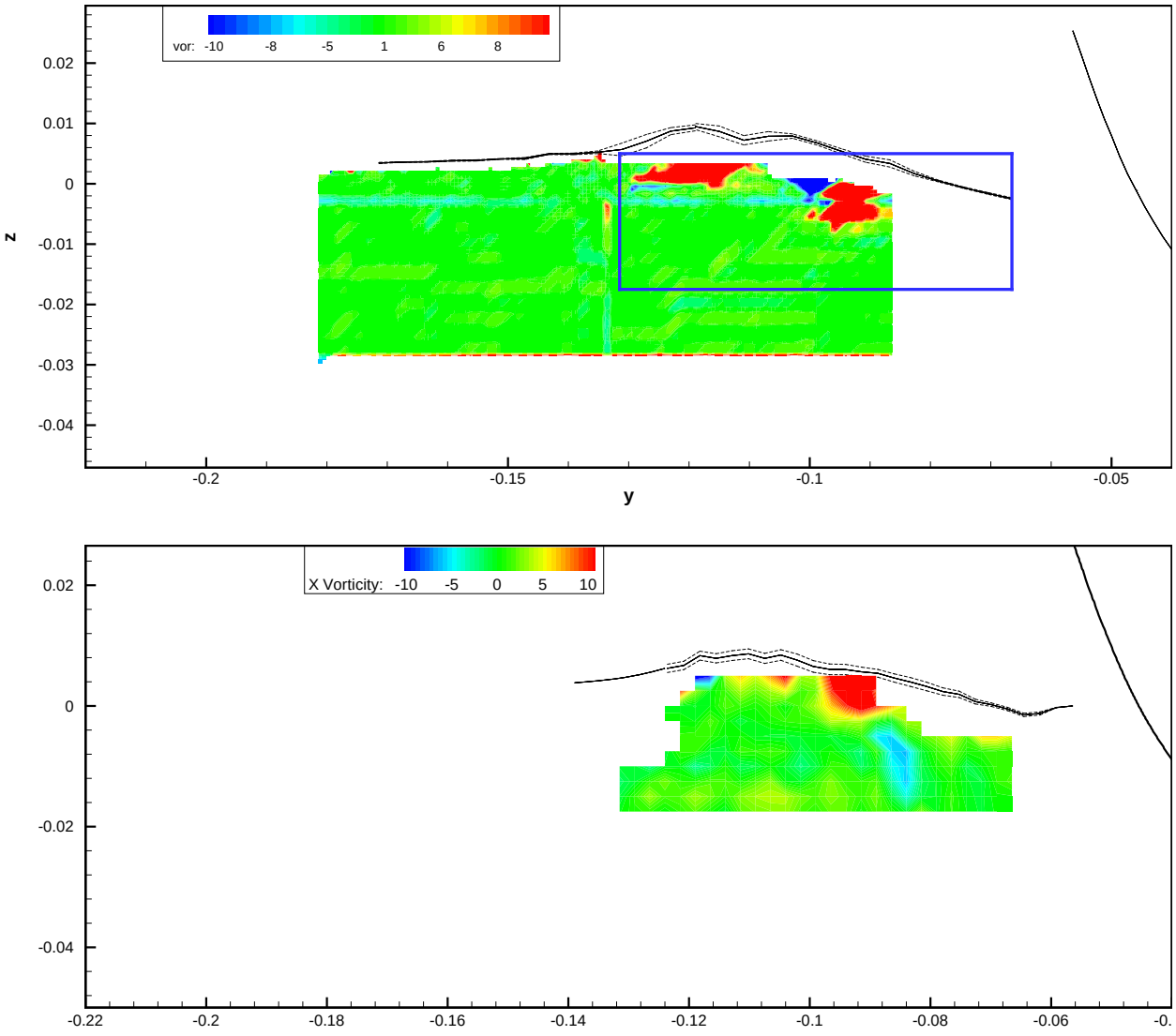

Figure 55: longitudinal vorticity maps for section 0.20 and for model C.2469 (top) and C.2340 (bottom). The data relative to C.2340 is taken from [37].

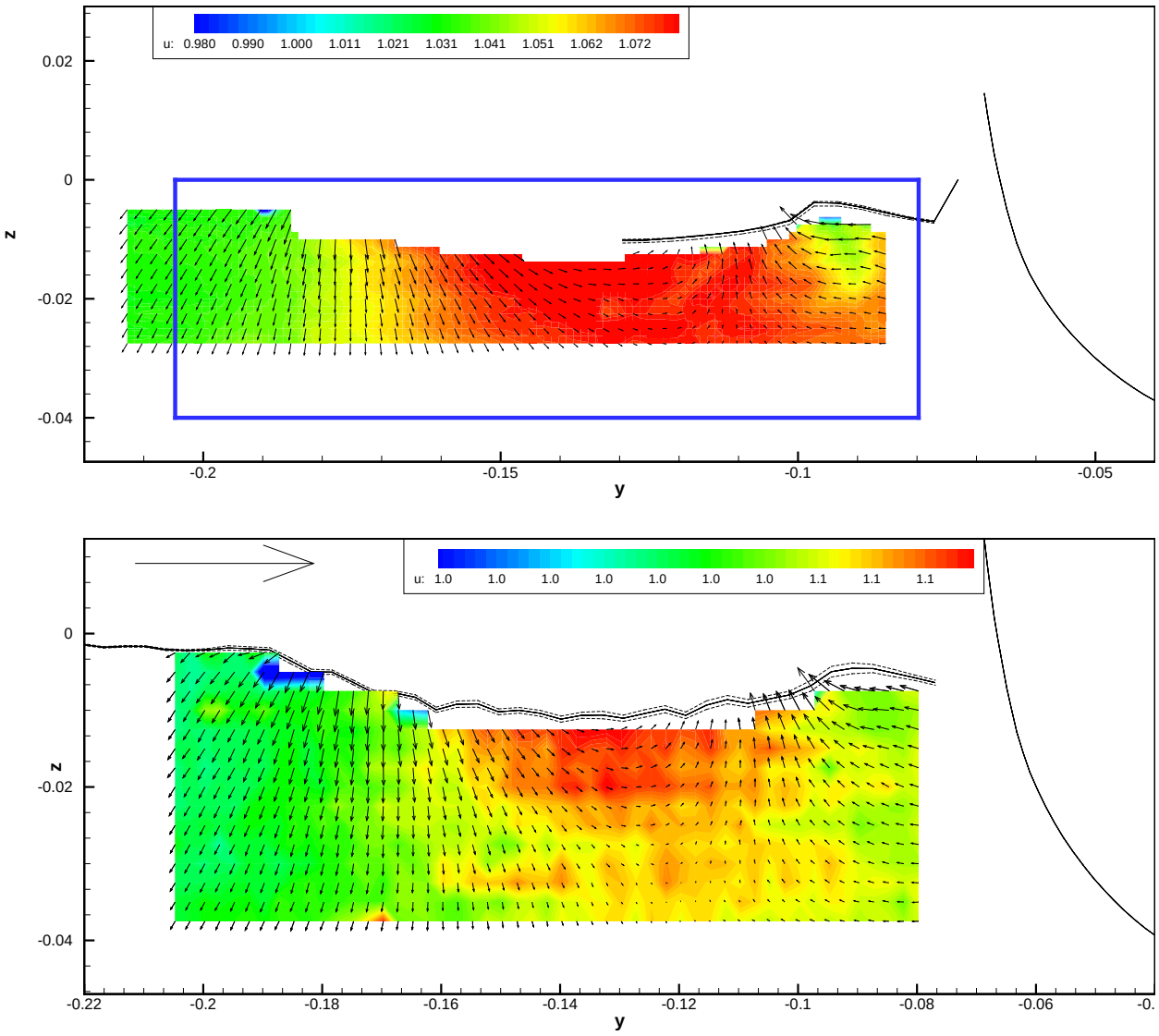

Figure 56: plots of measured velocity for section 0.40 Top frame: C.2469. Bottom frame: C.2340. The data relative to C.2340 is taken from [37].

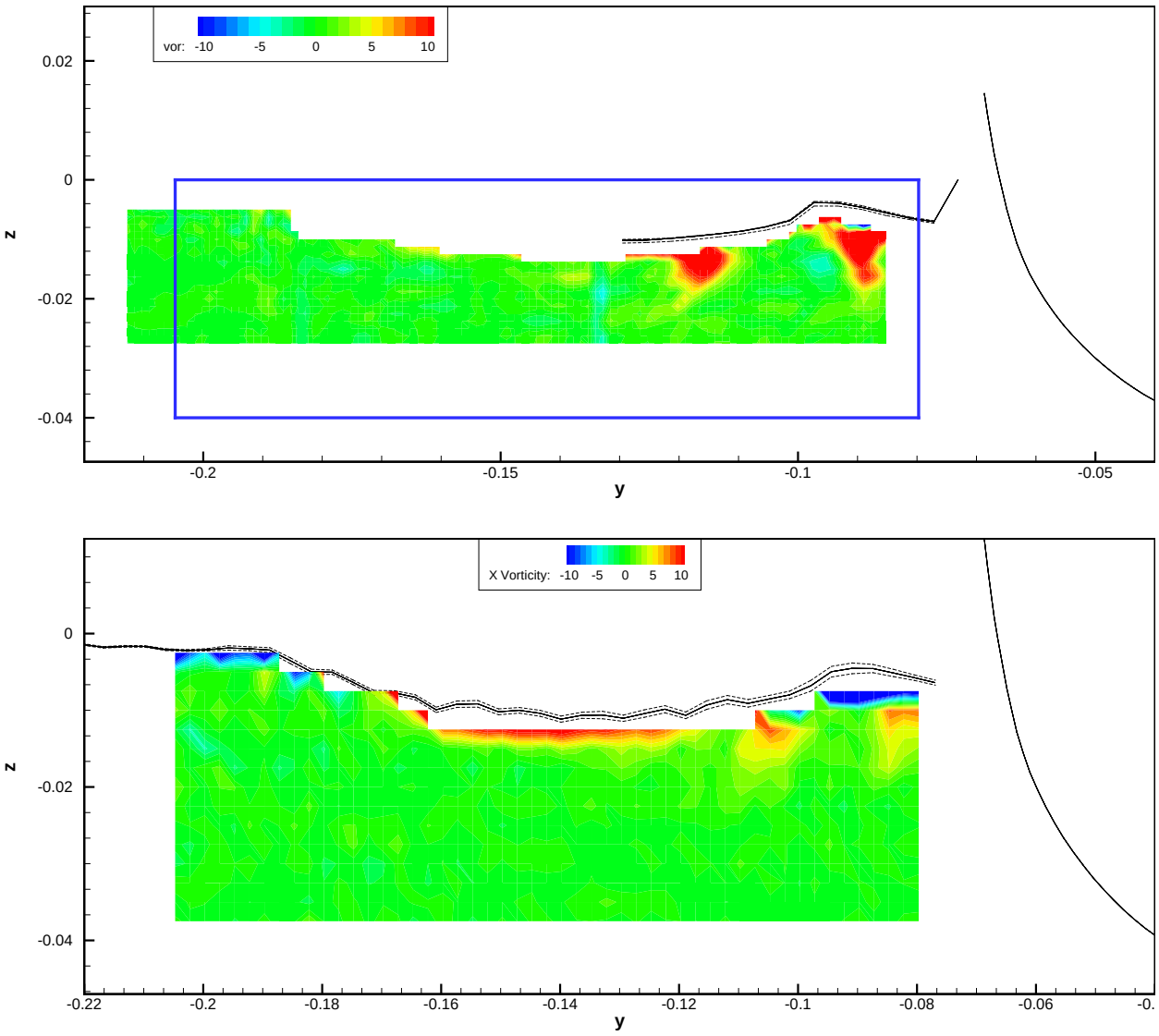

Figure 57: vorticity maps comparison for section 0.40, top frame is relative to C.2469 and bottom frame to C.2340. The data relative to C.2340 is taken from [37].

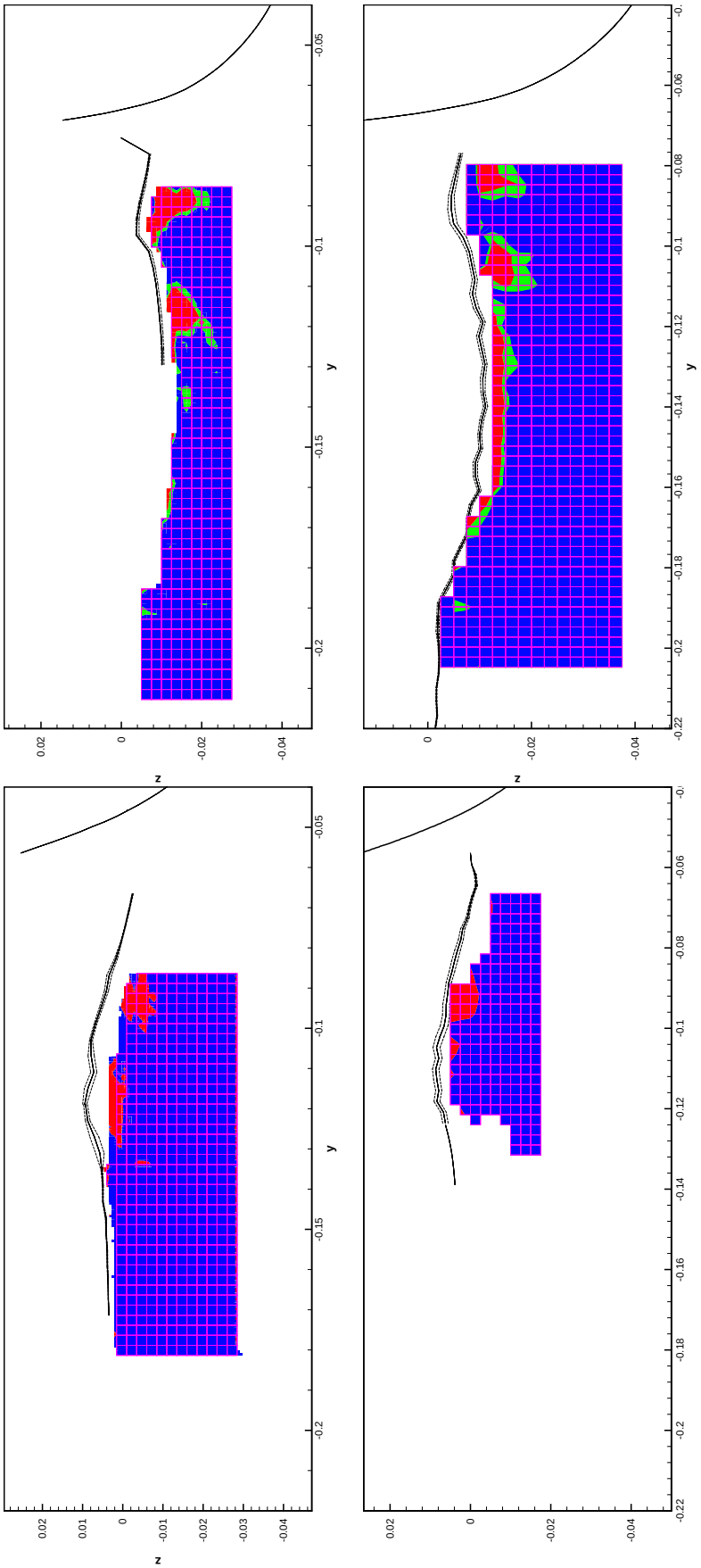

Figure 58: maps of vorticity above two common levels, in red is the area of vorticity above the value of 4 and in green the area of $\omega_x > 2$. Section 0.20 left column, section 0.40 right. Top row is relative to C.2469 while bottom row to C.2340. The data relative to C.2340 is taken from [37].

6 Conclusions

The resistance force relative to models of three different scales of the same ship have been measured during towing tank tests in a full range of Froude numbers.

The analysis of the results showed that the residual component of the total resistance coefficient has higher values in the case of the larger model for the fastest speeds. This increasing in the value of C_R has to be ascribed to the different breaking in the two cases. For the large model the breaking of the waves is not significantly influenced by surface tension.

The review of the pictures taken during the towing tests for the three model scales and for each test speed provide a qualitative description of the breaking modality. In the final part of the range of tested Froude numbers, let us say from Froude 0.20 up, the photographs show a substantial change of the breaking waves from one scale to the other for the same Froude number. The breakers of the small and middle model are clearly influenced by surface tension forces whereas the breaking relative to the large model is much more similar to the full scale one.

Local measurements of wave elevation in the near field of the model, for a given condition, namely Froude number of 0.35, and for the two larger models, confirm the difference in behavior of the breaking wave. The rms calculations from the wave elevation pattern show that the breaker of the larger model has a more stable configuration.

The comparison of the local flow field measured on two transversal sections for the two scales show that the overall flow map is similar. The calculations of vorticity

from the flow field measurements reveal that the bow breaking wave generates vorticity in the field. This vorticity is transported downstream by the mean flow in a series of distinct structured vortices with longitudinal axis. The vortices run very close to the free surface and traces can be also found in the surface scars where rms of surface elevation is high.

The vortices are one of the several mechanisms of energy dissipation related to the breaking waves. Although energy is dissipated in many other ways, such as spray generation and jet ejection, the comparison of the vorticity generated in the two scales show that the large model breaking generates a larger area of vorticity in the near filed of the model dissipating in this way more energy.

In conclusion experiments have been performed for a model scale that is able to reproduce the kind of breaking dynamic that can be seen in the full scale case that has been shown to be very different from common model scale breaking. Thus putting in evidence that the near field depends on the dimensions of the model. Vortical structures have been found in the near field of ships that is highly influenced by the breaking waves. One of the mechanisms of energy dissipation through breaking is dissipation through vorticity that has been found significantly increased in the larger model case due to the different dimensions of the produced breaking wave. This is one of the mechanism for energy dissipation and it is partially responsible to the difficulties in extending basin model test to the full scale.

Further developments should take into account the other sources of energy dissipation in the long waves breaking that till nowadays have not been quantified. The three-dimensional breaking wave still received very little attention by experimental researchers due to the measuring difficulties: the extreme velocity at which transient states occur, the great extent of the area interested by the breaking (we have seen that some breaking events can only take place at large scales), the great resolution needed to catch the turbulent motions in the breaker, the coexistence of two differ-

ent phases, liquid and gaseous. Thus an understanding of the basics mechanics of three-dimensional breaking and of its influence on the fluid dynamic field has still to be achieved thought this thesis can be a small step ahead on that direction.

7 Acknowledgements

The author of this thesis wishes to thank Dr. Emilio Campana who gave the impulse to this four years work and Dr. Angelo Olivieri for his highly competent scientific advices. Thanks also to Paolo Bulgarelli, our director in these years, that always supported my ambition to obtain the PhD.
Furthermore I wish to thank all the technicians and colleagues that helped me, very often physically speaking, with the huge model C.2469, too big to be handled by one person, in particular special thanks go to Giorgio Bartoccioni, the whole towing tank department and to the carpenters and mechanics of INSEAN.

It's the author's opinion that Peace between people is the fundamental value and that scientific research should be devoted to the human development and be diffuse to every one without patents, more in these sad days of war.
The fact that the hulls used in this job are warfare ship models demonstrate better that any word the painful situation that research is currently living, having to live on the money of the industry or, much worst, of the armies. Neither of these two subjects have anything to do with scientific research.
This thesis utilized warfare ship model as an example of modern ship conception, it has never been intended to be a work for military purposes, but exclusively devoted to a better understanding the mechanics of wave breaking and of the word that surrounds us.
The author never intended to be a direct or indirect accessory in the crime of developing a weapon.

Peace

References

[1] Baba E., (1969). *"A new component of viscous resistance of ships"*. Journal of Society of Naval Architects of Japan, vol 126.

[2] Banner M.L., Peregrine D.H., (1993). *"Wave breaking in deep water"*. Annual Review of Fluid Mechanics, vol.25 pp.373-97, Annual Reviews inc.

[3] Bonmarin P., (1989). *"Geometric properties of deep-waterbreaking waves"*. Journal of Fluid Mechanics, vol.209 pp.405-433, Cambridge University press.

[4] Kuang-An Chang, Philip L.-F. Liu, (1998). *"Velocity, acceleration and vorticity under a breaking wave"*. Physics of fluids, vol.10 (1) january, American Insitute of Physics.

[5] Ceniceros H.D., Hou T.Y., (1999). *"Dynamic generation of capillary waves"*. Physics of fluids, vol.11 (5) may, American Insitute of Physics.

[6] Coakley D., Duncan J., (1996). *"The flow field in steady breaking waves"*. Proc. of the 21st Symposium on Naval Hydrodynamics, Trondheim, Norway.

[7] Cointe R.,Tulin M.P., (1994). *"A theory of steady breakers"*. Journal of Fluid Mechanics, vol.276 pp.1-20, Cambridge University press.

[8] Dabiri D., Gharib M., (1997). *"Experimental investigation of the vorticity generation within a spilling water wave"*. Journal of Fluid Mechanics, vol.330 pp.113-139, Cambridge University press.

[9] Dias F., Kharif C., (1999). *"Nonlinear gravity and capillary-gravity waves"*. Annual review of fluid mechanics, vol.31 pp.301-346, Annual Reviews inc.

[10] Dong R.R., Katz J., Huang T.T. (1997). *"On the structure of bow waves on a ship model"*. Journal of Fluid Mechanics, vol.346 pp.77-115, Cambridge University press.

[11] Duncan J.H., (1981). *"An experimental investigation of breaking waves produced by a towed hydrofoil"*. Proceedings of Royal Society of London, vol.37 pp.331-384, Royal society London.

[12] Duncan J.H., (1983). *"The breaking and non-breaking wave resistance of a two-dimensional hydrofoil"*. Journal of Fluid Mechanics, vol.126 pp.507-20, Cambridge University press.

[13] Duncan J.H., Philomin V., Behres M., Kimmel J., (1994). *"The formation of spilling breaking water waves"*. Physics of fluids, vol. 6 (8) august pp.2258-2560, American Insitute of Physics.

[14] Duncan J.H., Dimas A.A., (1996). *"Surface ripples due to steady breaking waves"*. Journal of Fluid Mechanics, vol.329 pp.309-339, Cambridge University press.

[15] Duncan J.H., Qiao H., Philomin V., Wenz A., (1999). *"Gentle spilling breakers: crest profile evolution"*. Journal of Fluid Mechanics, vol.379 pp.191-222, Cambridge University press.

[16] Duncan J.H., Qiao H., (2001). *"Gentle spilling breakers: crest flow field evolution"*. Journal of Fluid Mechanics, vol.439 pp.57-85, Cambridge University press.

[17] Duncan J.H. (2001). *"Spilling breakers"*. Annual review of fluid mechanics, vol.33 pp.519-547, Annual Reviews inc.

[18] Fu T.C., Karion A., Rice J.R., Walker D.C., (2004). *"Experimental study of the bow wave of the R/V Athena I"*. Proc. of the 25th symposium on naval hydrodynamics, St.John's, Newfoundland and Labrador, Canada.

[19] Gui L., Longo J., Metcalf B., Shao J., Stern F., (2000). *"Forces, Moment and Wave Pattern for Naval Combatant in Regular Head Waves"*. Proc. of the 23rd symposium on naval hydrodynamics, Val de Reuil, France.

[20] Harvald SV. AA. (1983). *"Resistance and propulsion of ships"*. John Wiley and Sons.

[21] ITTC Recommended Procedures. (1999) *"Testing and Extrapolation Methods, General Density and Viscosity of Water"*. International Towing Tank Conference.

[22] ITTC Recommended Procedures. (1999) *"Testing and Extrapolation Methods Resistance Resistance Test"*. International Towing Tank Conference.

[23] Larsson L., Baba E. (1996). *"Ship resistance and flow computations"*. Advances in marine hydrodynamics, vol.5 pp.1-75, Computational Mechanics Publications, Southampton.

[24] Larsson, L., Stern F. and Bertram V., (2000). Editors *"Proceedings"*. Workshop on Numerical Ship Hydrodynamics, September, Gothenburg, Sweden.

[25] Larsson, L., Stern F. and Bertram V., (2003). *"Benchmarking of Computational Fluid Dynamics for Ship Flows: The Gothenburg 2000 Workshop"*. Journal of Ship Research, vol.47 n°1, pp.63-81 Soc Of Naval Arch & Marine Eng.

[26] Longo J., Stern F. (2003). *"Effects if drift angle on model ship flow"*. Experiments in Fluids, vol.32 pp.558-69, Springer.

[27] Longo J., Stern F. (2003). *"Uncertainty Assessment for Towing Tank Tests With Example for Surface Combatant DTMB Model 5415"*. Submitted Journal of Ship Research, 23 June 2003.

[28] Longuet-Higgins M.S., (1992). *"Capillary rollers and bores"*. Journal of Fluid Mechanics, vol.240 pp.659-79, Cambridge University press.

[29] Longuet-Higgins M.S., (1994). *"Shear instability in spilling breakers"*. Proceedings of Royal Society of London, vol.446 pp.399-409, Royal Society london.

[30] Miyata H., Inui T. (1984). *"Nonlinear ship waves"*. Advances in applied mechanics, vol.24 p.215, Academic press inc.

[31] Mui R.C.Y., Dommermuth D.G. (1995). *"The vortical structure of the parasitic capillary waves"*. Journal of Fluids Engineering, vol.117, ASME International.

[32] Peirson W.L., (1997). *"Measurements of surface velocities and shear at a wavy air-water interface using particle image velocimetry"*. Experiments in Fluids, vol.23 pp.427-437, Springer.

[33] Perlin M., Schultz W.W., (2000). *"Capillary effects on surface waves"*. Annual review of fluid mechanics, vol.32 pp.241-274, Annual Reviews inc.

[34] Olivieri A., Pistani F., Avanzini A., Stern F., Penna R. (2001). *"Towing tank experiments of resistance, sinkage and trim, boundary layer, wake, and free surface flow around a naval combattant INSEAN 2340 model"*. IIHR Technical report n 421. The University of Iowa, Iowa City, USA.

[35] Olivieri A., Pistani F., Penna R. (2003). *"Experimental investigation of the flow around a fast displacement ship hull model"*. Journal of Ship Research, vol.47, n°3, pp.247-261, Soc Of Naval Arch & Marine Eng.

[36] Olivieri A., Pistani F., Di Mascio A. (2003). *"Breaking wave at the bow of a fast displacement ship model"*. Journal of Marine Science Technology, vol.8 pp.68-75, Soc. of Naval Engineers of Japan.

[37] Olivieri A., Pistani F., Wilson R., Benedetti L., La Gala F., Campana E. F., Stern F. (2004). *"Froude number and scale effects and froude number 0.35 wave elevations and mean-velocity measurements for bow and shoulder wave breaking of surface combatant dtmb 5415"*. IIHR report, in preparation.

[38] Pogozelski E, katz J, Huang T, (1996). *"The shoulder wave separation generated by a surface piercing strut"*. Proc. of the 21st Symposium on Naval Hydrodynamics, Trondheim, Norway.

[39] Rapp R.J., Melville W.K., (1990). *"Laboratory measurements of deep-water breaking waves"*. phil. Trans. R. soc. Lond., vol.331 pp.735-800, The Royal Society Publications.

[40] Roth G.I., Mascenik D.T., Katz J. (1999). *"Measurements of the flow structure and turbulence within a ship bow wave"*. Physics of Fluids, vol.11 n.11, American Institute of Physics.

[41] Shakeri M., Liu X., Goll S., Duncan J. H. (2004). *"An experimental investigation of breaking bow waves simulated with a 2D+T technique"*. Proc. of the 25th symposium on naval hydrodynamics, St.John's, Newfoundland and Labrador, Canada.

[42] Stern F., Longo J., Penna R., Olivieri A., Ratcliffe T., Coleman H., (2000). *"International Collaboration On Benchmark Cfd Validation Data For Surface Combatant Dtmb Model 5415"*. Proc. of the 23rd symposium on naval hydrodynamics, Val de Reuil, France.

[43] Tulin MP. (1996). *"Breaking of theocean waves and downshifting"*. Waves and nonlinear processes in hydrodynamics. Kuwer Academic Publishers, The Netherlands

[44] Waniewsky Sur T., Chevalier K. (2004). *"Field measurements of bow spray droplets"*. Proc. of the 25th symposium on naval hydrodynamics, St.John's, Newfoundland and Labrador, Canada.